The discovery of aryl-2-nitroethyl triamino pyrimidines as anti-*Trypanosoma brucei* agents

Pasquale Linciano[a,1], Cecilia Pozzi[b,c], Giusy Tassone[b], Giacomo Landi[b], Stefano Mangani[b], Matteo Santucci[a], Rosaria Luciani[a], Stefania Ferrari[a], Nuno Santarem[d,e], Lorenzo Tagliazucchi[a,f], Anabela Cordeiro-da-Silva[d,e], Michele Tonelli[g], Donatella Tondi[a], Laura Bertarini[a], Sheraz Gul[i,j], Gesa Witt[i,j], Carolina B. Moraes[k], Luca Costantino[a], Maria Paola Costi[a,*].

[a]Department of Life Sciences, University of Modena and Reggio Emilia, Via Campi 103, 41125 Modena, Italy

[b]Department of Biotechnology, Chemistry and Pharmacy, University of Siena, Via Aldo Moro 2, 53100 Siena, Italy

[c]Consorzio Interuniversitario Risonanze Magnetiche di Metallo Proteine (CIMMP), Via Luigi Sacconi 6, 50019 Sesto Fiorentino (FI), Italy

[d]Institute for Molecular and Cell Biology, 4150-180 Porto, Portugal and Instituto de Investigação e Inovação em Saúde.

[e]Universidade do Porto and Institute for Molecular and Cell Biology, 4150-180 Porto, Portugal.

[f]Clinical and Experimental Medicine (CEM) PhD program, University of Modena and Reggio Emilia, Via Campi 278, 41125 Modena, Italy.

[g]Department of Pharmacy, University of Genoa, Viale Benedetto XV, 3, 16132 Genoa, Italy.

[i]Fraunhofer Institute for Translational Medicine and Pharmacology ITMP, Hamburg, Germany.

[j]Fraunhofer Cluster of Excellence for Immune-Mediated Diseases CIMD, Hamburg, Germany.

[k]Laboratório Nacional de Biociências (LNBio), Centro Nacional de Pesquisa em Energia e Materiais (CNPEM), 13083-100 Campinas - SP, Brazil; Present Address: Instituto Butantan & Department of Microbiology, Institute of Biomedical Sciences, University of Sao Paulo, 05508-900 Sao Paulo - SP, Brazil.

[1] Current affiliation: Department of Drug Sciences, University of Pavia, Via Taramelli 12, 27100- Pavia Italy.

[*] corresponding author

Abstract

Pteridine reductase 1 (PTR1) is a catalytic protein belonging to the folate metabolic pathway in Trypanosmatidic parasites. PTR1 is considered a target for the medicinal chemistry development of antiparasitic agents against Trypanosomiasis and Leishmaniasis. In previous studies, new nitro derivatives were elaborated as PTR1 inhibitors. The compounds showing a diammino-pyrimidine core structure were previously developed but they showed limited efficacy. Therefore a new class phenyl-, heteroaryl- and benzyloxy- nitro derivatives of the 2-nitroethyl-2,4,6-triaminopyrimidine scaffold were designed and tested. The compounds were assayed for their ability to inhibit *T. brucei* and *L. major* PTR1 enzymes and for their antiparasitic activity towards *T. brucei* and *L. infantum* parasites. To understand the structure-activity relationships of the compounds against *Tb*PTR1, the x-ray crystallographic structure of the 2,4,6-triaminopyrimidine (TAP) was obtained and molecular modelling studies were performed. As a next step, only the most effective *T. brucei* inhibitors were then tested against the amastigote cellular stage of *T. cruzi*, searching for a broad-spectrum antiprotozoal agent. An early ADME-Tox profile evaluation was performed. The early toxicity profile of this class of compounds was investigated by measuring their inhibition of *h*ERG and five cytochrome P450 isoforms (CYP1A2, CYP2C9, CYP2C19, CYP2D6 and CYP3A4), cytotoxicity towards A549 cells and mitochondrial toxicity. Pharmacokinetic studies were performed on selected compounds using hydroxypropyl-β-cyclodextrins (50% w/v) to preliminarily study the pharmacokinetic (SNAP-PK) (compounds administered in mice *per os* at a dose of 20 mg/kg). Finally, compound **1p** showing the optimal pharmacodynamic and pharmacokinetic properties was evaluated in a mouse model of *T. brucei* infection showing some efficacy up to 6 hours from the administration. Compound **1p** can be considered a good candidate for further bioavailability and efficacy studies.

Keywords

Drug Discovery, pteridine reductase, antiparasitic agents, *Trypanosoma brucei*, *Leishmania infantum.*

Introduction

Protozoan parasites represent a significant risk to health of billions world-wide and cause an estimated 810000 deaths annually [1], in addition to significant morbidity and large negative economic impact [2]. Among microparasites, Trypanosomatids are the etiologic agents of diseases such as leishmaniasis (caused by different species of Leishmania), Human African Trypanosomiasis (HAT, caused by *Trypanosoma brucei gambiense* and *rhodesiense*), and Chagas disease (caused by *T. cruzi*) [3,4]. Leishmaniasis is endemic in many tropical and sub-tropical countries and leading to approximately 1.3 million new cases of the disease and a mortality rate of 30,000 deaths per year [5]. On the base of morbidity and disability-adjusted life years (DALYs) leishmaniasis is considered to be as the third-most-common vector-borne disease after schistosomiasis and malaria [6]. The pathogen parasites (promastigotes) causing leishmaniasis are transmitted to mammalian hosts following a bite by infected sandfly which undergo cellular differentiation into amastigotes within mammalian macrophages. This eventually damages skin, mucosa or internal tissues and organs, causing cutaneous (CL), muco-cutaneous (MC) and visceral (VL) Leishmaniasis [7]. The last form is fatal in absence of treatment. Current therapies used to treat leishmaniasis include pentavalent antimonials, pentamidine, paromomycin, amphotericin B and miltefosine (MIL) which is the only oral agent. African trypanosomiasis, also known as African sleeping sickness, is caused by a parasitic protozoan of the genus *Trypanosoma*. The two forms, West African and East African trypanosomiasis, are caused by *Trypanosoma brucei gambiense* and *Trypanosoma brucei rhodesiense*, respectively [8]. *T. b. gambiense* accounts for more than 95% of cases and causes chronic infection which can emerge as severe disease many years after parasite infection [9]. *T. b. rhodesiense* causes acute infection, which can rapidly result in infection of the central nervous system when the parasites cross the blood–brain–barrier [10,11]. A third subspecies, *T. b. brucei*, is widely used in research owing to its non-pathogenicity to humans, while maintaining all the other characteristics of the two pathogenic species. The two species of *Trypanosoma* pathogenic to humans have different clinical manifestations with dissimilar course and severity [12]. *T. b. gambiense* is associated with a chronic form of the disease with a slower clinical course and a delayed manifestation compared to the time of infection [13]. *T. b. rhodesiense* is associated with a form of acute pathology with a faster course, and tendentially lethal within 2 weeks of infection [14]. In humans, the first manifestation of Human African Trypanosomiasis (HAT) occurs after a minimum of 5 days following inoculation and evolves in two distinct clinical phases: the first phase refers to the parasitic infection at the systemic level with symptoms overlapping with those of a common cold with fever, headache, and joint pain. The transition to the second phase takes several weeks (spp *rhodesiense*) or months (spp *gambiense*) after infection, when the parasite crosses the blood–brain–barrier via an unknown

mechanism, infecting the central nervous system [12,15]. The drugs used during the first stage of infection are pentamidine and suramin; the drugs used for the treatment of the second stage of the infection are mainly melarsoprol, eflornithine, and nifurtimox [5,16]. These parasitic infections are characterized by different phases and affect different organs during the course of the infections, therefore the currently used drugs do not fully meet the medical need and are characterized by heavy toxicity, limited efficacy and sometimes long periods of treatment. Many of them are used in therapy for over 50 years with the consequent appearance of resistance phenomena and treatment failure [17]. Thus, there is still a strong need for identifying new compounds active against Leishmania and Trypanosoma [16]. Studies performed on these parasites have shown that protozoa belonging to the genus Leishmania, and Trypanosoma are auxotrophic for folates and other pteridines are compounds necessary for the biosynthesis of nucleic acids and proteins [18]. These parasites have developed a sophisticated biochemical supply and reuse of these compounds from the infected host. This has made it possible to support the concept that pteridine reductase (PTR1), an enzyme that reduces the biopterins, could be a valid drug target for the treatment of Leishmaniasis and Trypanosomiasis [19]. The positive outcome from this approach could provide a valuable therapeutic option with respect to marketed drugs for Leishmaniasis and Trypanosomiasis.

PTR1 shows different functions in the Trypanosomatidic parasites yet to be completely disclosed [20,21]. Its role in the production of reduced pteridines is crucial to counterbalance the decrease activity of dihydrofolate reductase (DHFR) when the antifolates are delivered to the parasites. It was proven to be essential through genetic methods. Some inhibition strategies are directed to target both DHFR and PTR1 metabolic reactions to exclude the cross talk among the respective pathways, that allows the recovering of some metabolic activity after inhibition [19]. The known enzymatic reaction reported in Figure 1 shows how the pterin reduction pathway provides tetrahydrobiopterin that is useful for different pathways including the quinoid dihydrobiopterin and tetrahydrobiopterin-carbinolamine reactions [21]. The reduction steps involving PTR1 can also transform folate to dihydrofolate and then to tetrahydrofolate. When the parasitic DHFR is inhibited due to antifolates treatment, PTR1 is overexpressed to contribute to the pteridine reduction pathway balancing the DHFR block. The crosstalk between the biopterin and pteridines pathways is a matter of study today.

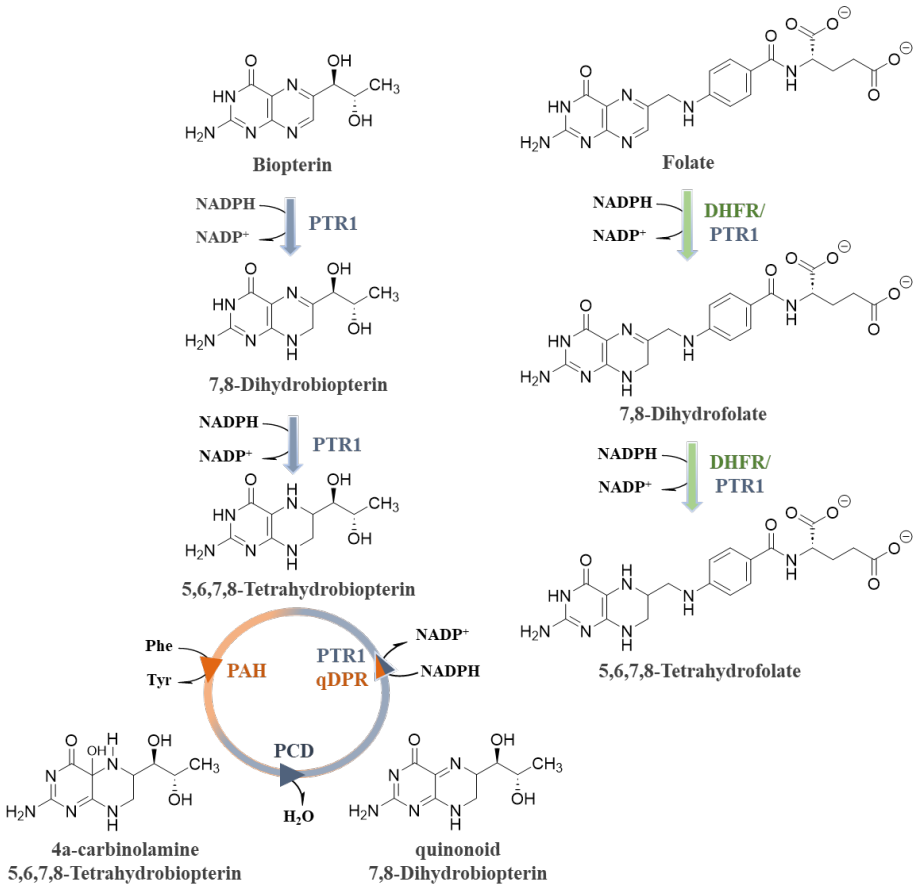

Figure 1. Biopterin and folate metabolic pathways. Enzymes present in both *Trypanosoma* and *Leishmania* parasites are shown in light blue or green, those only present in *Leishmania* spp are shown in orange. PAH, phenylalanine-4-hydroxylase; Phe, phenylalanine; Tyr, tyrosine; PCD, pterin-4a-carbinolamine dehydratase; qDPR, quinonoid dihydropteridin reductase.

PTR1 inhibitors present a wide range of different scaffolds showing a similar mechanism consistent with competition with the biopterin substrate [22]. Pyrimidines are known privileged structures in drug discovery, as they resemble the nucleobases and when included in bicyclic systems, such as pteridines and biopterins, they can replace the cofactor metabolites and occupy the respective binding sites in the enzymes catalytic site. The pyrimidine core shows different substitution sites that permit to control selectivity and physicochemical properties of the title compounds due to an appropriate functionalization [23]. Hunter *et al*. described the antiparasitic activity of some nitroalkylpyrimidines, prepared as chemical intermediates of pyrrolopyrimidines, targeting the parasitic pteridine reductase 1 (PTR1). In particular, four 2,4,6-triaminopyrimidine derivatives (compounds **D1**-**D4**, Figure 2) were found to be active in *in vitro* against *T. b. brucei*, with an IC_{50} in the low micromolar range [24]. However, these compounds exhibited a poor inhibitory activity against *Tb*PTR1 in the high micromolar range thus reasonably assuming that other pathways and targets could be involved in their mechanism of action.

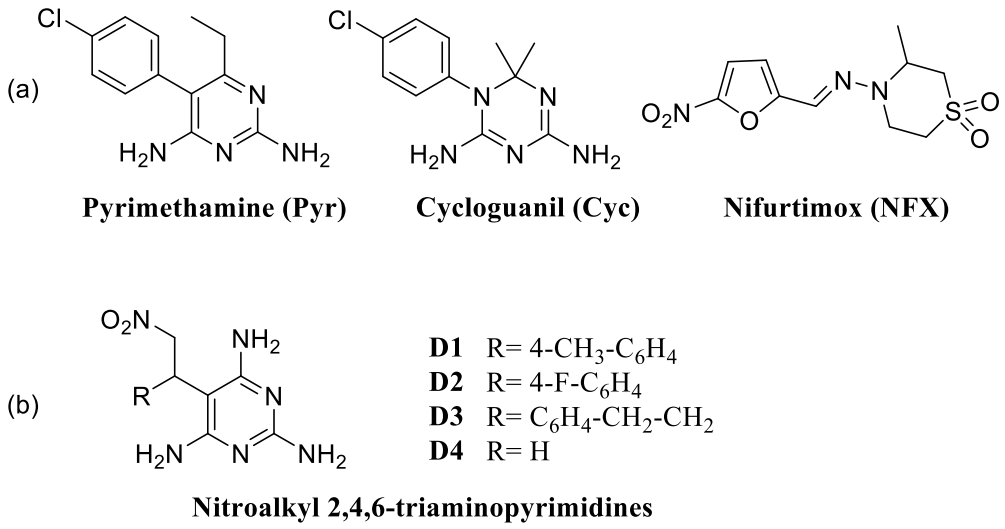

Figure 2. (a) Antiprotozoal drugs incorporating a pyrimidine ring (pyrimetamine, **Pyr**) or an isostere thereof, dihydrotriazine, (cycloguanil, **Cyc**) or a nitrofuran group (nifurtimox, **NFX**), as key chemical features for the activity; (b) previously reported anti-*Trypanosoma brucei* agents (**D1**-**D4**), combining the triamino pyrimidine core with a nitro group, sharing marginal activity *versus* PTR1 [24].

The aim of the present work is to expand the **D1**-**D4** class of derivatives, to increase their inhibition potency against PTR1 and their antiparasitic activity. The 2-nitroethyl-2,4,6-triaminopyrimidine scaffold was decorated with phenyl-, heteroaryl- and benzyloxy- fragments (see Table 1). The compounds were assayed for their ability to inhibit *T. brucei* and *L. major* PTR1 enzymes and for their antiparasitic activity towards *T. brucei* and the amastigote form of *L. infantum* parasites. To understand the on-target structure-activity relationships, the X-ray crystallographic structure of the 2,4,6-triaminopyrimidine (**TAP**) was obtained and molecular modelling studies were performed. As a next step, only the most effective *T. brucei* inhibitors were tested against the amastigote cellular form of *T. cruzi*, searching for a broad spectrum antiprotozoan agent. The toxicity of the compounds towards THP-1 human macrophages was evaluated due to the importance of the cells in the body immune reactivity. The CC_{50} (concentration of compound able to produce the half of the maximal concentration showing non-toxic effects) was taken as a parameter of reference for the toxicity of the compounds against human cells and used to calculate the Selectivity Index (SI), the ratio between CC_{50} and the EC_{50} (compound concentration causing the inhibition of the 50% of the cell growth). To further investigate the early toxicity profile of this class of compounds, inhibition of *h*ERG and five

cytochrome P450 isoforms (CYP1A2, CYP2C9, CYP2C19, CYP2D6 and CYP3A4), cytotoxicity towards A549 cells and mitochondrial toxicity were assessed.

Pharmacokinetic studies were finally performed on selected compounds showing a suitable ADME-Tox profile, in complex with hydroxypropyl-β-cyclodextrins (50% w/v). A preliminarily snapshot PK approach (SNAP-PK) (compounds administered in mice *per os* at a dose of 20 mg/kg) was performed to limit the animal overuse. Finally, the compound with the optimal pharmacodynamic and pharmacokinetic properties was evaluated in a mouse model of *T. brucei* infection.

Results and Discussion

Compounds design

The design of the 5-(2-nitro-1-arylethyl)-2,4,6-triaminopyrimidines was based on the X-ray crystallographic complex of *Tb*PTR1-**Pyr** (PDB ID: 7OPJ [19]) in which the diamino pyrimidine ring resembles the **TAP** structure. The X-ray crystal structure shows **Pyr** in the active site of the *T.brucei* binding at the biopterin site. the pyrimidine ring is sandwiched between the cofactor nicotinamide and Phe97, forming an array of hydrogen bonds with catalytic residues and the cofactor phosphate and ribose (Figure 3). Visual inspection of the crystallographic complex suggests that alkyl-aryl substituents can be added in position 5 of the pyrimidine ring to reach either the hydrophobic pocket S1, lined by Val206, Leu209, Pro210, Met213, and Trp221, or the more hydrophilic pocket S2, lined by Cys168, Glu161, Phe171, and Tyr 174. Figure 3 shows the direction of fragment growing out of position 5 of the pyrimidine ring towards the pockets S1, in orange, and S2, in blue.

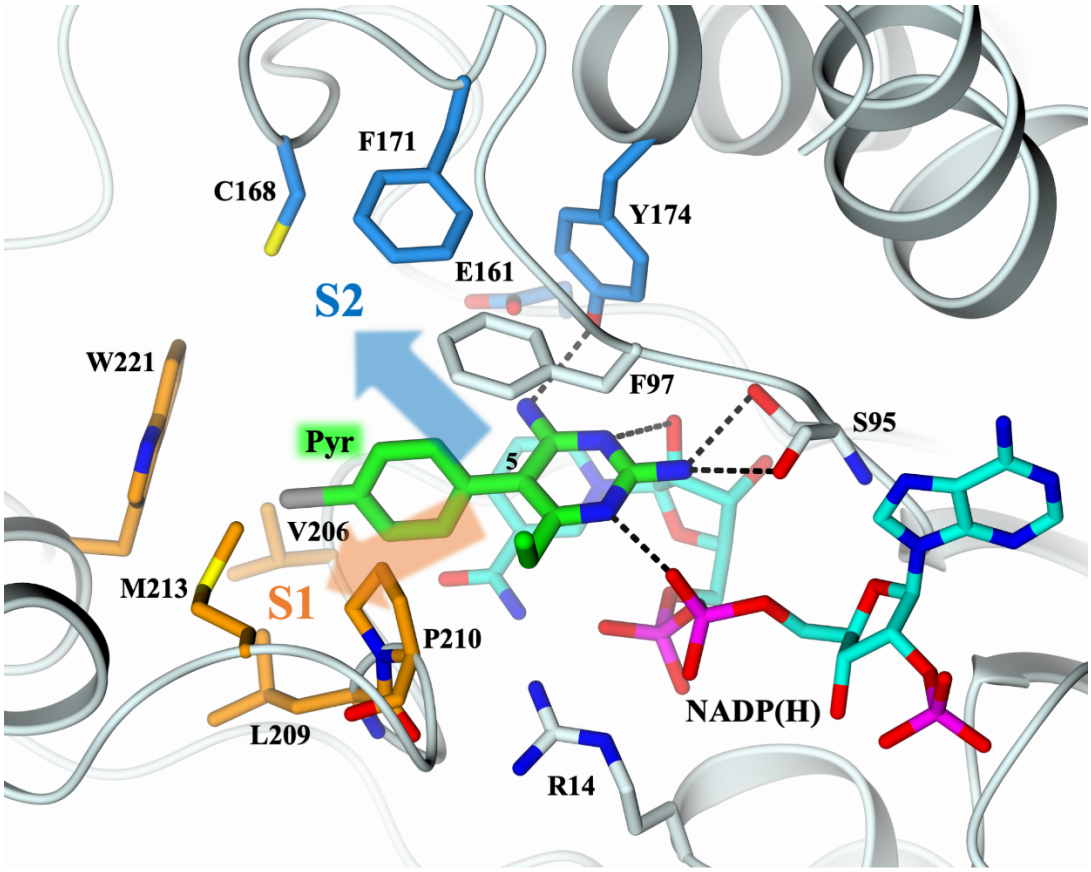

Figure 3. X-ray pose of **Pyr** (in stick, green carbons) in the *Tb*PTR1 active site (light cyan cartoon and carbons; NAPD(H) in stick, cyan carbons; PDB ID:7OPJ [19]). The cofactor NAPD(H) is shown in stick (cyan carbons) and the **Pyr** H-bonds with the catalytic residues and the cofactor as black dashed lines. The hydrophobic pocket S1, lined by Val206, Leu209, Pro210, Met213, and Trp221, is highlighted in orange whereas the more hydrophilic pocket S2, lines by Cys168, Glu161, Phe171, and Tyr 174, in colored blue. The two arrows (color-coded as the targeted pockets) indicate the directions of fragment growing out of position 5 of the pyrimidine ring.

Chemistry

The 5-(2-nitro-1-arylethyl)-2,4,6-triaminopyrimidines **1a-q** and **2a-e** were obtained in good yield (45-70 %) and purity (>95 %), by Michael's addition of 2,4,6-triaminopyrimidine to the appropriate nitro-styrene derivative (**3a-q** and **4a-e**) in water/ethyl acetate 1:1 (v/v) at 60 °C, overnight. Nitro-styrenes **3a-q** were synthesized starting from the respective commercially available aryl-carboxaldehyde with refluxing nitromethane (Henry reaction), using ammonium acetate as a buffering agent. For the synthesis of the intermediate nitro-styrenes **4a-e**, the proper benzyloxy-benzaldehydes (**5a-e**) were initially prepared by reacting the hydroxy-benzaldehyde with the

appropriate benzyl chloride in standard S_N2 conditions (**Scheme 1**). All the compounds were characterized by NMR and MS. Purity (>98%) was assessed thought HPLC-UV/Vis analysis.

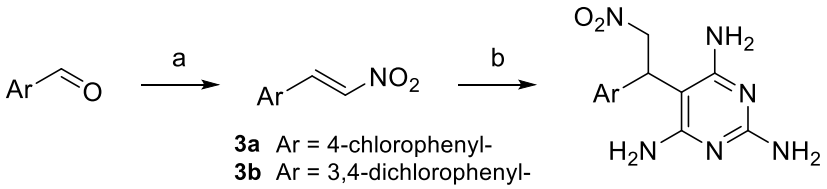

1a-q, 2a-e

3a Ar = 4-chlorophenyl-
3b Ar = 3,4-dichlorophenyl-
3c Ar = 4-bromophenyl-
3d Ar = 3-bromophenyl-
3e Ar = 3-nitrophenyl-
3f Ar = 3,4-dimethoxyphenyl-
3g Ar = 3-methoxy-4-hydroxyphenyl-
3h Ar = 2,6-dimethoxyphenyl-
3i Ar = 2-furyl-
3j Ar = 2-thiophenyl-
3k Ar = 2-(5-methyl)thiophenyl-
3l Ar = 4-chlorophenyl-
3m Ar = 5-benzo[d][1,3]dioxolyl-
3n Ar = 4-benzo[d][1,3]dioxolyl-
3o Ar = 2,3-dihydro-5-benzofuryl-
3p Ar = 3-benzo[d]thiophenyl-
3q Ar = 1H-3-indolyl-

4a Ar = 2-(3,4-dichlorobenzyloxy)phenyl-
4b Ar = 2-(benzyloxy)phenyl-
4c Ar = 2-(2-nitrobenzyloxy)phenyl-
4d Ar = 2-(3-chlorobenzyloxy)phenyl-
4e Ar = 4-(3,4-dichlorobenzyloxy)phenyl-

Scheme 1. Reagents and conditions: **a.** NH_4AcO (1.5 eq.), nitromethane, reflux, 6 h, 75-90 % yield; **b.** 2,4,6-triaminopyrimidine (1 eq.), H_2O/AcOEt 1:1, 60 °C, overnight, 45-70 % yield.

PTR1 inhibitory activity

All 22 new 1-aryl-2-nitroethyl pyrimidines **1a-q** and **2a-e** were initially screened at 50 μM for their inhibitory activity against *T. brucei* and *L. major* PTR1 enzymes. The two enzymes share 50% amino acid sequence similarity and comparisons indicate that the architecture of the cofactor binding site, and the catalytic core are highly conserved [23]. Compounds yielding >80 % inhibition of *Tb*PTR1 and *Lm*PTR1 were profiled in dose-response experiments (compound concentrations from 0.10 to 100 μM) to determine their potencies. These results are shown in Table 1, in comparison with those of **TAP**, as the fragment of reference present in all the investigated derivatives, **Pyr** and pentamidine, as reference drugs.

Table 1. Compound inhibition data (IC_{50}) of 5-(1-aryl-2-nitroethyl) pyrimidines-2,4,6-triamine **1a-q** and **2a-e** towards *Tb*PTR1 and *Lm*PTR1.

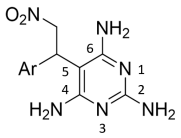	**Ar**	***Tb*PTR1**	***Lm*PTR1**
		IC_{50} (μM)[a]	
1a	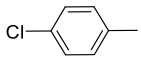	<0.10[c]	ND[b]
1b	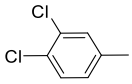	0.15	60.2
1c	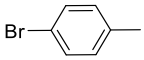	<0.10[c]	64.1
1d	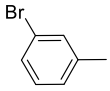	0.05	58.1
1e	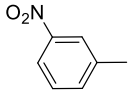	<0.10[c]	63.4
1f	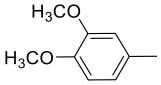	0.12	2.4
1g	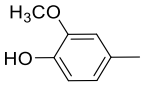	0.07	19.8
1h	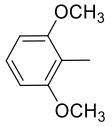	0.13	70.7
1i		0.16	63.8
1j		0.19	4.90
1k	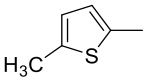	0.39	ND[b]
1l	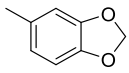	0.25	ND[b]
1m	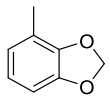	0.03	47.6
1n	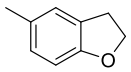	0.39	21.3

1o	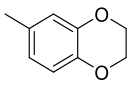	0.23	2.50
1p	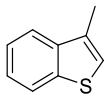	0.30	47.4
1q	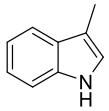	<0.10[c]	13.9
2a	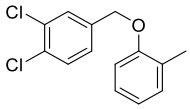	0.27	46.0
2b	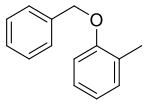	0.24	51.3
2c	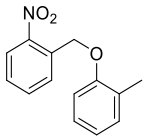	0.26	46.2
2d	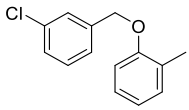	0.60	51.3
2e	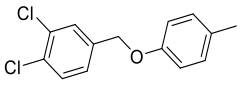	0.22	49.7
TAP	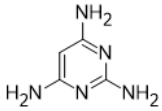	2.38	4.01
Pyr	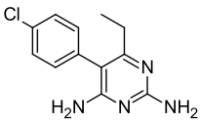	0.09	13.6
Pentamidine	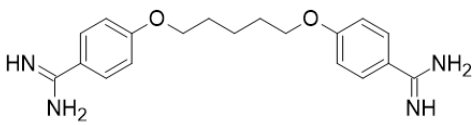	77.9	87.1

[a]Data are representative of three independent experiments and are expressed as means or % of inhibition (errors on IC_{50} are within 10 %); [b]ND: not detectable (no inhibition at 50 μM); [c] the shape of the dose-response effect allowed only an IC_{50} estimation.

All tested compounds were proven to be active against the PTR1 enzymes from both species (*T.brucei* and *L.major*) and in some cases with improved potencies relative to the reference compound **Pyr** (Table 1). It is also noteworthy that *Trypanosoma brucei* is more sensitive to this class of compounds with many compounds associated with sub-micromolar potencies. On the other hand, the activity of 2,4,6-triaminopyrimidine is comparable for *Tb* and *Lm*PTR1. Inhibition of PTR1 activity is mainly driven by the 1-aryl-2-nitroethyl pyrimidine structure and decoration/disposition of substituents on the aromatic/heteroaromatic moiety.

Structural analysis of *Tb*PTR1 in complex with the 2,4,6-triaminopyrimidine

Different attempts to obtain the X-ray crystal structure of the synthesized compounds could not provide any results. Therefore, **TAP**, the scaffold of the compounds library synthesized, was tested, and the structure of the ternary complex *Tb*PTR1-NADP(H)-**TAP** was solved at 1.48 Å resolution (Table S1, Table S2). The crystal asymmetric unit includes a whole *Tb*PTR1 tetramer, representing the functional assembly of the enzyme. The overall structure of *Tb*PTR1 is highly conserved with those previously described [19]. The four subunits were completely traced apart for two surface-exposed loops, including residues 104–113 and 143–151, usually poorly ordered in *Tb*PTR1 structures [25]. The cofactor NADP(H) binds to the enzyme in an extended conformation, stabilized by a tight network of conserved H-bonds [25]. The formation of the holoenzyme is essential for creating both the catalytic site and the substrate binding pocket, where the pterin moieties of the substrates and substrate-like inhibitors bind in a peculiar π-sandwich between the nicotinamide ring of NADP(H) and the aromatic side chain of Phe97 (Figure 4a) [26]. Within the *Tb*PTR1 catalytic cavity, the substrate and cofactor molecules are further stabilized by the interactions entailed with the flexible substrate-binding loop, including residues 207-215.

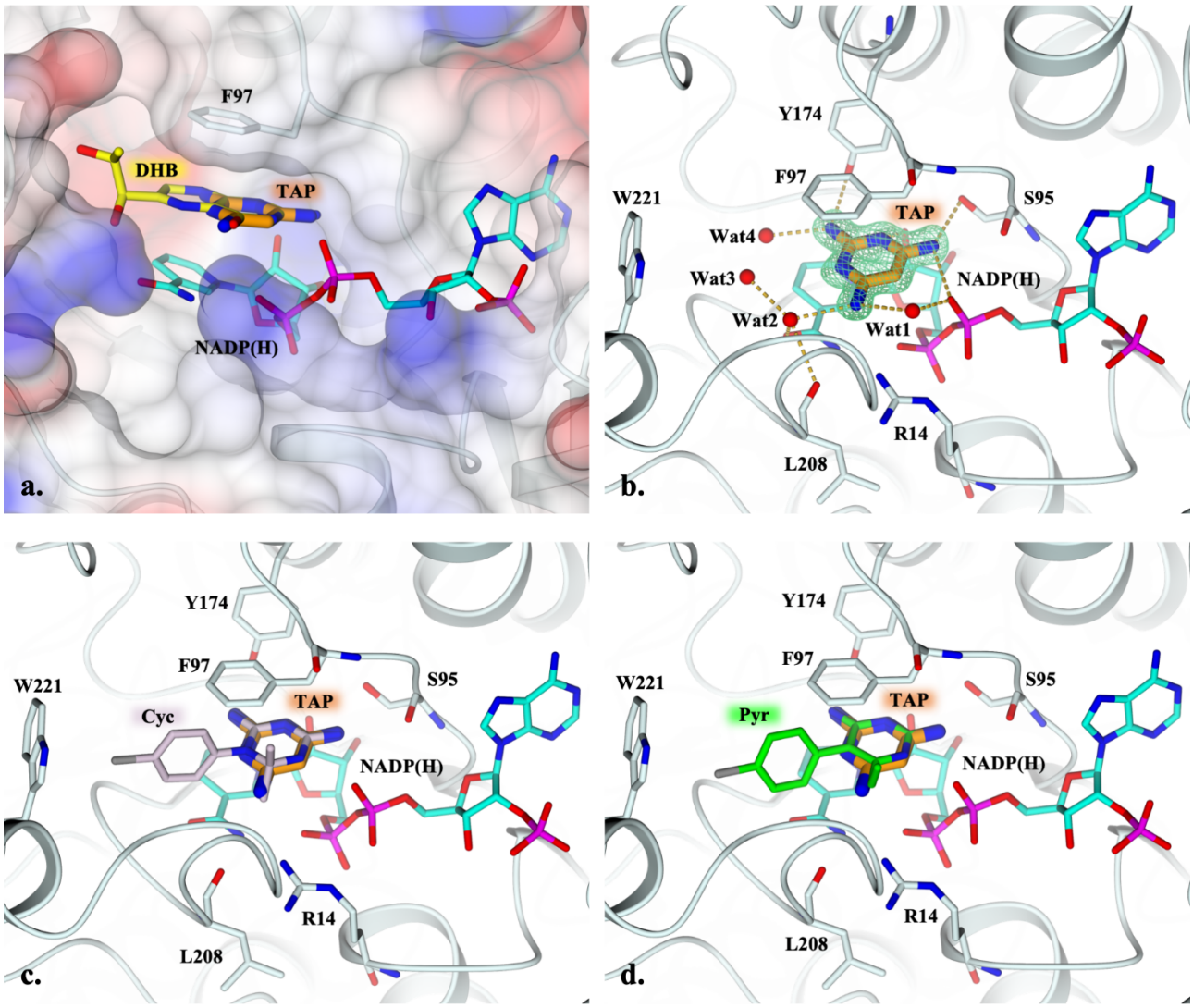

Figure 4. a. Active site view of *Tb*PTR1 (transparent electrostatic surface, light cyan cartoon and carbons) in complex with the cofactor NAPD(H) (in stick, cyan carbons), and **TAP** (in sticks, orange carbons), overlapped with the structure of the complex *Lm*PTR1-NAPD(H)-dihydrobiopterin (DHB, in sticks, yellow carbons; PDB id 2BF7 [26]). Substrate and substrate-like inhibitors bind in a peculiar π-sandwich between the nicotinamide ring of NADP(H) and the aromatic side chain of Phe97. For clarity, only the substrate is displayed in the complex *Lm*PTR1-NAPD(H)-DHB, whereas, in the structure of *Tb*PTR1, the segment 205-215, covering the biopterin-binding pocket, is not shown; **b**. Binging interaction of **TAP** (surrounded by the omit map, green mesh, contoured at the 3σ level) within the *Tb*PTR1 active site. Hydrogen bonds are displayed as orange dashed lines and water molecules as red spheres (arbitrary radius); **c,d**. Active site view of the superimposition with the complexes **c**) *Tb*PTR1-NADP(H)-cycloguanil (**Cyc**, in sticks, lilac carbons; PDB id 6HNC [27] and **d**. *Tb*PTR1-NADP(H)-pyrimethamine (**Pyr**, in sticks, green carbons; PDB id 7OPJ [19]). The binding mode of **TAP** matches those of the analogous moieties of **Cyc** and **Pyr**. In all panels, oxygen atoms are colored red, nitrogen blue, phosphorous magenta, and chlorine grey.

In the structure of the complex with **TAP**, the presence of the inhibitor was detected in the active site of all subunits of the *Tb*PTR1 tetramer, where it occupies the biopterin-binding pocket, stacked in the peculiar Phe97 – NADP(H) nicotinamide π-sandwich (Figure 4a). Inside the cavity, **TAP** is further stabilized by a tight network of conserved H-bonds with the cofactor and the surrounding residues exposed in the active site (Figure 4b). The amine moiety in positions 2 of the **TAP** pyrimidine ring donates a H-bond to Tyr174. The **TAP** pyrimidine nitrogen in position 3 accepts a H-bond from the NADP(H) ribose hydroxyl, whereas its C(4) amine moiety donates two H-bonds to Ser95 and the cofactor β-phosphate. Additional water mediated interactions are formed by the amine moiety at the **TAP** C(6) with both the cofactor β-phosphate (Wat1, Figure 4b) and the Leu208 backbone carbonyl (Wat2, Figure 4b). The binding mode of **TAP** closely resembles those formerly described for the analogous moieties of **Cyc** (Figure 4c) and **Pyr** (Figure 4d) and of pyrimidine-based inhibitors [19,27]. The X-ray complex PTR1:**TAP** represents a structural reference for the development of new compounds including the same core fragment.

Structure-activity relationships based on molecular docking studies

Molecular docking studies were performed to elucidate how the ligands complement the active site of PTR1 and to investigate the binding interactions at the base of the enzyme inhibitory potency of most active compounds. All the 22 derivatives underwent docking studies, as well as **Pyr** and **TAP** that contain the diamine-pyrimidine fragment present also in all 1-aryl-2-nitroethyl pyrimidine derivatives herein reported. Simulations were performed using the coordinates deriving from the binary complex of *TbPTR1* with **Pyr** (PDB ID: 7OPJ [19]), in comparison with *Tb*PTR1:**TAP** complex, using the Extra Precision (XP) Glide implemented in the Schrodinger LLC suite, version 2022-2 (Schrödinger LLC, New York, USA [27,28]). The designed docking procedure was previously validated by redocking the co-crystallized **Pyr** in the active site of the enzyme, resulting in an optimal superposition between the X-ray structure and the predicted one (Figure S1). Extra Precision (XP) ligand docking against *Tb*PTR1 predicted the active ligands could fit appropriately in the active site and establish valuable interactions with the surrounding residues as discussed hereafter, and with the pyrimidine core closely resembling the available crystallographic orientation of **Pyr**. For compounds shown in **Table 1**, the pyrimidine ring assumes an orientation closely like that assumed by **Pyr** and **TAP** in their respective crystallographic complexes. Overall, for most of the candidates, the amine moiety at C(2) of the pyrimidine ring H-bonds to the Ser95 hydroxyl and backbone carbonyl groups. The pyrimidine nitrogen atoms in position 1 and 3 directly interact with the cofactor, forming H-bonds with the ribose hydroxyl and β-phosphate groups, respectively.

Noteworthy the amine moiety at C(4) H-bonds to the Tyr174 hydroxyl group, that is further H-bonded with the Asp161 carboxylate [23], a key interaction within the *Tb*PTR1 catalytic cavity, playing a prominent role during catalysis. Additionally, the pyrimidine core of the present inhibitors binds through the peculiar π-sandwich between the cofactor NADPH and the aromatic side chain of Phe97, as previously mentioned for **Pyr** (Figure 5).

The nitroethyl group is generally positioned in a subpocket delimited by Val206, Leu209, Pro210, Met213 and Trp221 (subpocket S1, Figure 6), eventually interacting with the latter through two π-cation contacts. Other frequent interactions involve hydrophobic contacts between the aromatic substituent and Pro210, Phe97, Trp221, Cys168 and Met213 residues. Additionally, the aromatic or heterocyclic rings (Ar moiety in Table 1) of the inhibitors are usually involved in π–π stacking interactions with Phe97 and/or Trp221.

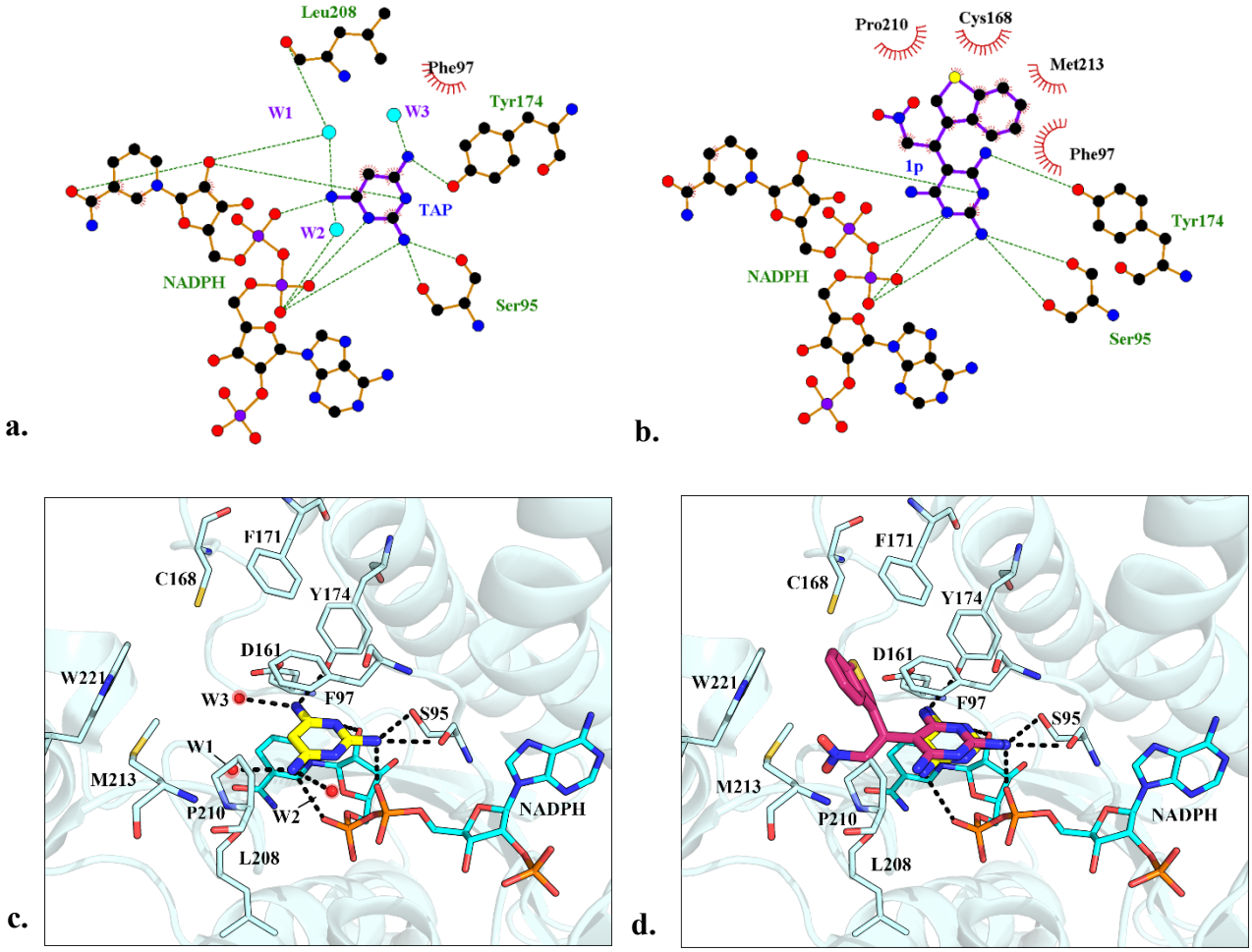

Figure 5. **a.** Binding interactions of **TAP** in *TbPTR1* active site (PDB ID: 8OF2); **b.** Binding interactions of candidate **1p** docked in *TbPTR1* active site; **c**. Tri-dimensional crystal pose of TAP in

TbPTR1 active site (PDB ID: 8OF2); **d.** Comparison of the crystal pose of TAP (yellow) and the docked compound **1p** (magenta). The compounds, cofactor NADPH (cyan) and residues that line the pocket are shown as capped sticks. Figures **a** and **b** were prepared with LigPLOT [29]. Figures **c** and **d** was prepared with PyMOL (PyMOL Molecular Graphics System, Version 2.5 Schrödinger, LLC) [30].

The docking models obtained for the compounds are discussed below and the corresponding figures are reported in Supporting Information section, as mentioned below. For the halogen para-substituted candidates **1a** and **1c (**IC_{50} <0.10 μM**)** (Figure S2a, S2c) the pyrimidine core slightly deviates from the orientation experimentally observed for **Pyr** (IC_{50} 0.09) and **TAP**, weakening the interactions with Ser95 and Tyr174, but **TAP** remains less active than **Pyr** and **1a** and **1c**. The introduction of a substituent in meta of the aryl ring, as for compounds **1b** and **1d** (IC_{50} of 0.15 μM and 0.05 μM respectively) (Figure S2b, S2d), allows a better accommodation of the ligands in the binding site, enhancing the key interactions between the pyrimidine moiety and Ser95/Tyr174, as seen for **Pyr** and **TAP**. However, the presence of a chlorine atom in para (**1b**) results in steric clashes with Trp221 and Cys168 that does not significantly alter its affinity, when compared to the halogen meta-substituted candidate **1d**. The presence of a bulkier group in meta position in the aryl ring as the nitro moiety of compound **1e** (Figure S3a), results in the orientation of the aryl and the nitroethyl group towards a solvent-exposed region delimited by hydrophobic residues and this geometry change does not affect the affinity of **1e** with respect to **1a** and **1c**. Candidates **1f** and **1g (**IC_{50} 0.12 μM and 0.07 μM) (Figure S3b, S3c), accommodate in the binding site adopting two possible orientations: the methoxy group in meta alternatively points towards an inner subpocket enclosed by Cys168, Phe97, Phe171, Tyr174 and Asp161 (subpocket S2; Figure 6) or a more solvent exposed region. In both cases, they establish favorable interactions between the pyrimidine core and the aforementioned serine and tyrosine residues, as well as NADPH. Overall, the presence of a solvent exposed hydroxyl in para (**1g)** does not change significantly the inhibitory activity compared to the bulkier methoxylated analogue **1f** despite the possible clash with the bridge formed by Trp221 and Cy168. Interestingly, the introduction of a more cumbersome substituent in ortho position, as for **1h** (Figure S3d), leads to the rotation of the molecule by orienting one of the methoxy groups towards the hydrophobic cavity S1 and the nitro moiety in a S2 subpocket; this rotation results in a loss of interaction between the pyrimidine and Ser95, while other key contacts are maintained and overall, no IC_{50} change (0.13 μM).

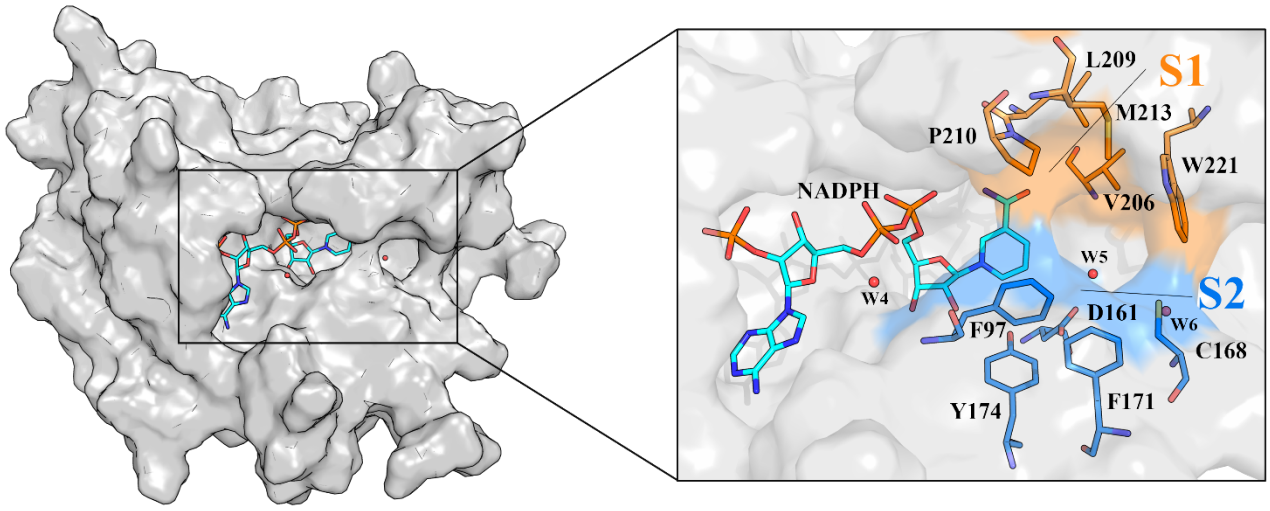

Figure 6. Organization of the *Tb*PTR1 active site. A surface representation of the *Tb*PTR1 subunit with cofactor NADPH (cyan) bound and three water molecules (PDB ID: 7OPJ) with a zoom on the two subpockets S1 (orange) and S2 (blue). Residues that line the cavity and cofactor are shown as capped sticks, water molecules as red spheres. Figures were prepared with PyMOL (PyMOL Molecular Graphics System, Version 2.5 Schrödinger, LLC) [30].

The pyrimidine core of heterocycle-substituted candidates **1i** and **1j** traces the key stabilizing interactions previously observed for **Pyr** and **TAP**-derivatives; the only difference between these two candidates is the opposite orientation of the furan/thiophene and nitroethyl moiety towards S1/S2 subpockets (Figure 7). The binding pose of **1k** (Figure S4a) closely resembles that assumed by its analogue **1j**, but the introduction of a methyl on the thiophene moiety causes steric hindrance without affecting the inhibitory potency (IC_{50} = 0.39 μM for **1k** with respect to 0.19 μM for **1j**).

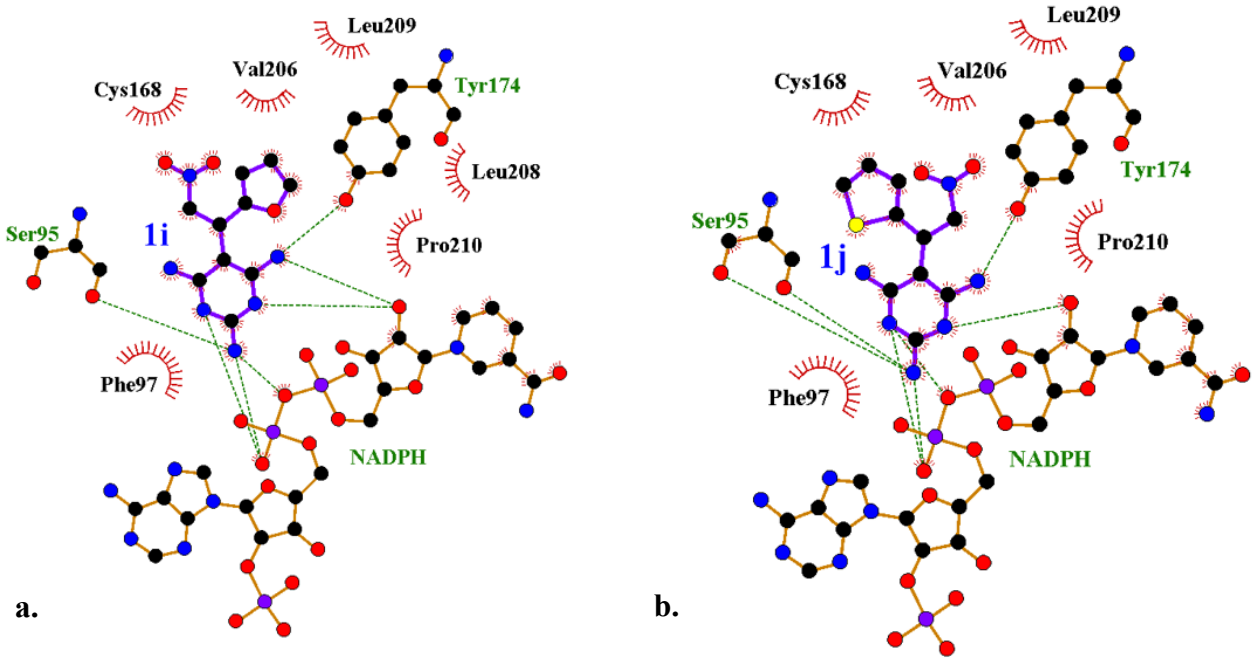

Figure 7. **a.** Binding interactions of **1i** docked in *TbPTR1* active site; **b.** Binding interactions of candidate **1j** docked in *TbPTR1* active site. The candidate is shown in purple lines, NADPH and residues involved in H-bonds with the ligand are reported in orange. H-bonds are represented as dashed green lines, while residues involved in hydrophobic contacts are shown as red semi-circles. Figures were prepared with LigPLOT [29].

According to the *in vitro* experimental data, candidates **1l**, **1n** and **1o** (Figure S4b, S4c, S4d) exhibit comparable potency (IC_{50} between 0.23 to 0.39 μM, Table 1): these compounds share similar binding pose characterized by the orientation of the nitroethyl moiety in the S1 subpocket described above and the accommodation of the aromatic substituent in a solvent accessible channel enclosed by Phe97, Pro210, Cys168 and Trp221. Compound **1m**, the most active *Tb*PTR1 inhibitor (IC_{50} 0.03 μM) shows the same interactions pattern so far reported for the pyrimidine core and the nitroethyl moiety, while the benzodioxolyl substituent in ortho, alternatively pointing towards S2 or a solvent-accessible area, allows the formation of a stabilizing intramolecular H-bond and an optimal occupation of the binding site (Figure 8a) that support the 10-fold IC_{50} increase compared to **1l**.

The docking procedure predicted that **1p** is embedded within the binding site by several H-bonds involving the amino-pyrimidine core, the cofactor NADPH and residues Ser95 and Tyr174, as well as the peculiar π-sandwich between the cofactor NADPH and the aromatic side chain of Phe97. Additionally, the positioning of the nitroethyl moiety in the S1 subpocket allows the establishment of π-cation interactions with the aromatic residue Trp221 (5.6-6.2 Å), while the benzothiophene ring

is oriented towards the hydrophobic S2 (Figure 5b). **1p** shows similar IC_{50} compared to **1n** and **1o** bearing a similar double ring heterocyclic moiety (**1p** IC_{50} = 0.30). The afore-mentioned interactions pattern is retraced by candidate **1q** where the thiophene moiety is replaced by an indole motif (Figure S4e) and this shows an apparent similar IC_{50} compared to **1p**. In both cases (**1p** and **1q**) the heteroatom does not establish specific interactions with the enzyme residues thus supporting the similar binding pattern.

Interestingly, among the benzyloxyphenyl derivatives, the introduction of a bulkier and flat substituent result in a higher number of π-stacking between the Ar moiety and the aromatic residues in the binding site Phe97, Phe171, Trp221, however resulting in a variable displacement of the pyrimidine core. For candidates **2b** (Figure S5b) and **2d** (Figure 8b), the pyrimidine moiety, despite its slight rotation compared to **TAP** orientation (1.2 Å), maintains key stabilizing interactions with NADPH, Ser95 and Tyr174, while the positioning of nitroethyl in S1 subpocket results in weak π-cation contacts with Trp221 (6.4-6.6 Å) and Phe97 (6.3 Å). The structural similarity between these two compounds results in superimposable docking poses characterized by the benzyl (**2b**) and 3-chlorobenzyl (**2d**) rings forming extra π–π stacking with Phe97 and Phe171 and, overall, the presence of a chlorine atom doesn't distort the binding orientation since it turns out to be solvent-exposed and shows a similar IC_{50} (**2b** IC_{50}=0.24 μM and **2d** IC_{50} 0.60 μM).

Differently, the introduction of bulkier substituents as in **2a** and **2c (**IC_{50}=0.27 μM and 0.26 μM**,** respectively) (Figure S5a, S5c) leads to a re-orientation of the molecule with the Ar moiety embedded in S1 establishing π–π stacking with Trp221 (5.0-5.3 Å) and the nitroethyl group pointing toward S2 subpocket interacting with Phe171 (5.6 Å). The latter residue is also involved in the formation of stabilizing π–π contacts with the chlorobenzyl and nitrobenzyl rings, belonging to **2a** and **2c** respectively. As previously mentioned, the presence of cumbersome groups leads to a displacement of the pyrimidine core thus losing contact with Ser95 and weakening those with NADPH and Tyr174. Similarly behaves candidate **2e** (Figure S5d), whose pyrimidine moiety is shifted compared to **TAP** losing the key interactions, while ensuring a better accommodation within the binding site, featured by the occupation of the S1 subpocket by the nitroethyl and the positioning of the Ar group in the channel delimited by Phe97, Pro210, Cys168 and Trp221.

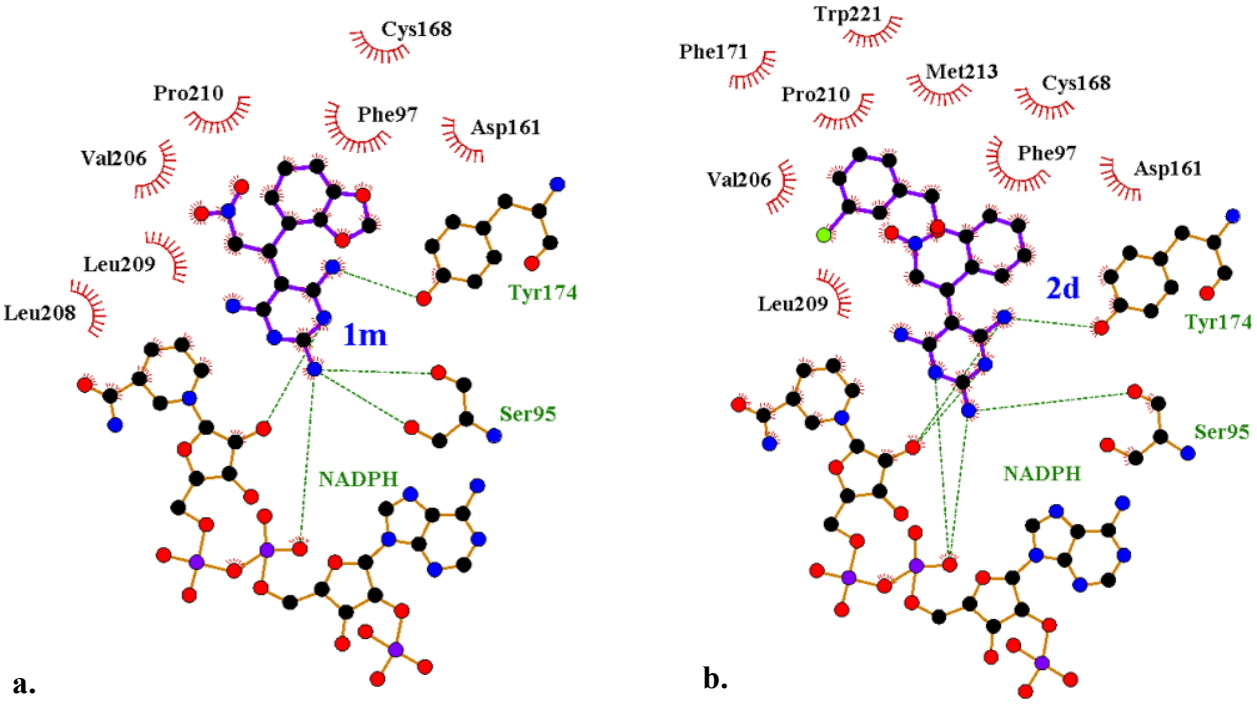

Figure 8. **a.** Binding interactions of **1m** docked in *TbPTR1* active site **b.** Binding interactions of candidate **2d** docked in *TbPTR1* active site. The candidate is shown in purple lines, NADPH and residues involved in H-bonds with the ligand are reported in orange. H-bonds are represented as dashed green lines, while residues involved in hydrophobic contacts are shown as red semi-circles. Figures were prepared with LigPLOT [29].

In vitro anti-parasitic screening

The synthesized 1-aryl-2-nitroethyl pyrimidines **1a-q** and **2a-e** were evaluated first for their in vitro anti-parasitic activities against cultured bloodstream form of *T. brucei.* To evaluate the potential broad-spectrum anti-trypanosomatidic activity, all compounds were screened against the intracellular amastigote stage of *L. infantum*. We employed resazurin-based approach for the screening, that enables robust anti-parasitic evaluation using bloodstream forms. The anti-parasitic potential of this class of compounds against *T. brucei* was evaluated by reporting the EC_{50} when the cell growth inhibition at 10 μM was higher than 50%, for the less active molecules it only reported activity at 10 μM (Table 2). The intracellular amastigote form of *L. infantum* was used as a more physiological cellular model of the infection and this increases the difficulty of the identification of new anti-*Lehismanial* compounds because more membrane barriers should be crossed to reach the intracellular form of the parasite. Compounds with more than 80% activity at 50 μM in this intracellular model,

underwent dose-response experiments for the determination of their potency (EC_{50}) (**Table 2**). Pentamidine was used as reference compound in *T. brucei* assay, exhibiting an EC_{50} 3.8 nM which is comparable with the value reported in the literature [31], whereas miltefosine was utilized as positive controls in the *L. infantum* assay yielding an EC_{50} of 1.29 μM [32]. The complete antiparasitic profiling against *T. brucei* and *L. infantum* is reported in Table 2.

Table 2. Anti-parasitic activities[a] against *T. brucei*, and the amastigote form of *L. infantum* of 1-aryl-2-nitroethyl pyrimidines **1a**-**q** and **2a**-**e**.

Compound	*T. brucei*			*L. infantum*
	EC_{50} μM	CC_{50} range[b]	SI	% inhibition at 50 μM
1a	1.28	]50;25[	19	ND
1b	0.82	]50;25[	31	53.9
1c	1.59	]50;25[	16	83.4
1d	0.65	]100; 50[	118	30.2
1e	1.19	]100; 50[	42	74.2
1f	2.33	]50;25[	11	62.4
1g	2.13	]100; 50[	23	21.6
1h	1.68	]25; 12.5[	7	79.8
1i	5.05	]100; 50[	10	ND
1j	3.33	]100; 50[	15	22.5
1k	2.41	100	42	15.4
1l	0.50	]50;25[	50	ND
1m	1.21	]25; 12.5[	10	36.0
1n	4.40	]100; 50[	11	21.1
1o	1.11	]25; 12.5[	11	54.4
1p	0.09	]25; 12.5[	139	49.0

1q	28 % at 10 µM	ND	ND	4.0
2a	0.30	]50;25[	83	11.7
2b	0.60	>100	167	81.1
2c	48 % at 10 µM	ND	ND	11.7
2d	0.40	]25; 12.5[	31	61.0
2e	0.34	]100; 50[	147	11.4
Pentamidine	0.0038	-	-	-
Miltefosine	-	-	-	1.29

[a]Data are representative of three independent experiments and are expressed as means or % of inhibition (errors on EC_{50} are within 10 %); [b] The toxicity was determined using an approach in which we report the last non-toxic concentration using for concentrations 100, 50, 25,12,5. N.D.= Not Determined, means no detectable data at the measured concentration.

Almost all the tested 1-aryl-2-nitroethyl pyrimidines yielded a complete cell growth inhibition against *T. brucei* at the tested concentration, resulting in an EC_{50} ranging from 90 nM (for **1p**) to 5.05 µM (for **1i**). Only **1q** and **2c** were an exception due to their low anti-*T. brucei* activity since the percentage of cell growth inhibition was of 28 % and 48 % at 10 µM, respectively. These two unexpected results could be reasonably ascribed to the poor solubility/bioavailability. Conversely, no compounds showed an appreciable anti-parasitic activity against the intracellular form of *L. infantum* (% cell growth inhibition <74 % at 50 µM, Table 2) and, therefore they were not considered for further studies against this parasite. In addition, the most active compound against *T. brucei* (**1p,** EC_{50} 90 nM) was tested against the intracellular amastigote stage of *T. cruzi*, to probe its potential activity toward other parasitic species. Interestingly, compound **1p** showed the ability to inhibit *T. cruzi* parasites with an EC_{50} 14.1 µM. Thus, **1p** was the best performing compound in the series, being endowed with a broad anti-parasitic activity (*T. brucei* EC_{50} 0.09 µM and *T. cruzi* EC_{50} 14.1 µM). As an added value, the potency of **1p** against the two Trypanosoma parasites was in the low micromolar IC_{50} range (*T. cruzi* EC_{50} 2.4 µM). The IC_{50} values against PTR1 enzymes and the EC_{50} against *L. infantum* and *T. brucei* were reported in a graphical representation in Figure **9a** and **9b**. The corresponding data are reported in Table S3 and Table S4.

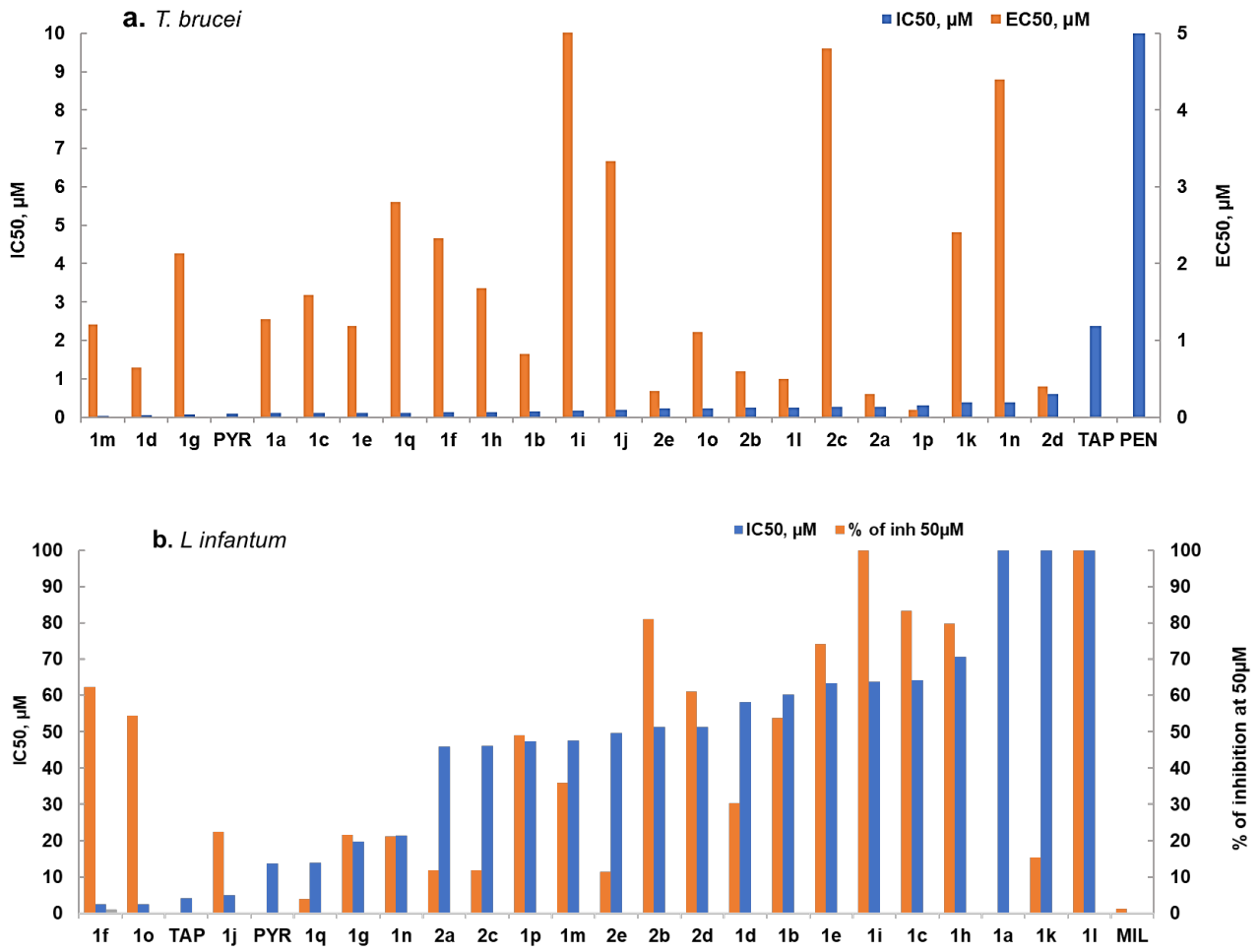

Figure 9. a. Comparison of IC_{50} between *Tb*PTR1 and EC_{50} from dose-response experiments in *T. brucei* parasites; **b.** Comparison of IC_{50} between *Lm*PTR1 and the % of inhibition of *L. infantum* parasites at 50µM.

Early ADME-Toxicity Studies

Early ADME-toxicity studies were performed for all compounds that were synthesized with the aim to identify liabilities and to select the safest and most active for progression in the drug discovery value chain. Cytotoxicity studies were the first to be performed against THP-1 macrophages, commonly used to grow protozoan parasites (**Table 2**). Cytotoxicity was expressed as CC_{50} corresponding to the concentration of compound able to produce the half of the maximal concentration showing non-toxic effects (**Table 2**). Moreover, the compounds were assessed for cardiac toxicity by measuring the inhibitory effect on the *h*ERG ion-channel, inhibition of representative cytochrome P450 isoforms, mitochondrial toxicity, and for cytotoxicity against A549 human lung carcinoma cells. Compounds were screened at 10 µM, and the results are reported as %

inhibition (Figure 10a) and compared with their EC_{50} **(**Figure 10b**)** where the ratio between the percentage of inhibition of metabolic enzymes and their antiparasitic activity are reported. Figure 10b better represents the ADME-Tox profile of the compounds.

Figure 10. a. Early-Toxicity studies Heatmap representing the % inhibition for the investigated compounds (at 10 µM) against *h*ERG, five CYP450 isoforms, mitochondrial toxicity and cytotoxicity against the A549 cell-line (or cell inhibition for hA549 line). Data are representative of three independent experiments and are expressed as % of inhibition (errors are within 10 % of the mean data); **b.** HeatMap representing the selectivity index (S.I.) between the percentage of inhibition of metabolic enzymes and their antiparasitic activity. S.I. is expressed as the ratio between the inverse

of mean CYP inhibition and EC_{50} on *T. brucei*, i.e. values were obtained by subtracting to 100 the percentage of enzyme inhibition, and this number was divided by their EC_{50} (namely, [(100-% enzyme inhibition) / EC_{50}]. Higher values (green cells, >1) represent non-toxic compounds, where red cells (values >10) represent the most toxic compounds. Values < 0% of enzyme inhibition were reported as 0.01, while values >100% were reported to 100. The corresponding data are reported in Table S3 and S4. The Heatmap are obtained with Excel 2022 by input of a three-color legenda with the mean colour being at the half of the interval for figure **a**, and at 10% of the scale for figure **b**, respectively.

Apart from **1a**, **1e**, **1n**, **2b** and **2c**, none of the compounds exhibited toxicity against *h*ERG, which is a pivotal parameter for proceeding a compound further in the drug discovery process (Figure 10a). This profile remains similar only for compounds **1n**, **2a** and **2c** from SI reported in Figure 10b. In contrast, a significant inhibition of at least one of the CYP450 isoforms was observed in all the compounds, especially considering CYP1A2 and CYP2D6. Only compounds 1m was associated with mitochondrial toxicity as shown in Figure 10b. Importantly, no significant cytotoxicity was detected against the A549 cell-line for all compounds (yellow tiles in Figure 10a) apart from **2c** and **2e** that were cytotoxic (Figure 10a). From Figure 10b, **1p** and **2e** are the least toxic compounds with respect to their EC_{50}. The toxicity profile of the two best performing compounds (**1p** and **2e**) against *T. brucei* in terms of anti-parasitic activity and SI respect with THP-1 cell-line was in-depth investigated, determining the IC_{50} against *h*ERG, CYP isoforms and mitochondria, and the GI_{50} against A549 cell line. The selectivity index for each toxicity parameter was calculated (Table 3), as the ratio between the IC_{50} or GI_{50} and the antiparasitic EC_{50} showed against *T. brucei*.

Table 3. Early-toxicity profile of compounds **1p** and **2a** against some key targets and corresponding SI with respect to the EC_{50} against *T.brucei*.

Cmp	*T. b.* EC_{50} (µM)	*h*ERG IC_{50} (µM) [SI]	1A2 IC_{50} (µM) [SI]	2C9 IC_{50} (µM) [SI]	2C19 IC_{50} (µM) [SI]	2D6 IC_{50} (µM) [SI]	3A4 IC_{50} (µM) [SI]	A549 GI_{50} (µM) [SI]	Mitotoxicity IC_{50} (µM) [SI]
1p	0.09	16.0 [178]	3.0 [33]	24.4 [271]	15.3 [170]	10.2 [113]	>100 [>1100]	10.6 [117]	10.4 [115]
2a	0.3	>100 [>300]	1.2 [4]	3.2 [11]	8.0 [26]	5.9 [20]	5.9 [20]	10.0 [33]	3.9 [13]

Importantly, **1p** and **2a** elicited additional interest for their general low toxicity (**Table 3**) leading to corresponding high values of SI, which depict a wide therapeutic window for this class of compounds. Accordingly, SI was used as a key parameter for the qualitative selection of the dose of the compound necessary to achieve the desired pharmacological effect and minimal toxicity, as discussed in the subsequent *in vivo* tests.

Pharmacokinetics evaluation and *in vivo* study on infected mice

Based on the anti-parasitic *vs.* toxicity profile of the tested compounds, **1m**, **1o**, **1p**, **2a**, **2d**, **2e** were selected for *in vivo* studies since they were the most promising for the treatment of *T. brucei* infection. The selection was based on the ADME-Tox selectivity (Figure 10b) and EC_{50} observed against *T.brucei* (Table 3). Before proceeding to test the anti-parasitic activity in mice models, preliminary pharmacokinetic studies in healthy BALB/c mice, using a SNAP-PK approach, were performed. **2a** was chosen as pilot compound and was initially assessed IV at 1 mg/kg and *per os* at 20 mg/kg. However, **2a** in both routes of administration was not able to reach a plasmatic concentration above its anti-parasitic EC_{50} (0.30 μM), and after 1 hour it was no more detectable in plasma (data not shown). The low plasmatic level of **2a** could be due to the low water solubility of the compound. Due to the structural similarity, also compounds **1m**, **1o-p**, **2d-e** are expected to behave in the same way. With the aim of improving solubility and the oral bioavailability, **2a** and other selected compounds (**1m**, **1o-p**, **2d-e**) were complexed with hydroxypropyl-β-cyclodextrin (HP-β-CD) and administered *per os* at the dose of 20 mg/kg. Plasma samples were taken at 30, 45 minutes and 1, 3, 24, 48 and 72 h after administration. The plasmatic concentration was quantified by LC-qqqMS (Figure 11). The plasmatic profile and the key pharmacokinetic parameters are reported in Figure 11 and Table 4, respectively. The samples analysis was interrupted after 24 hours, because all compounds did not show a detectable plasma concentration.

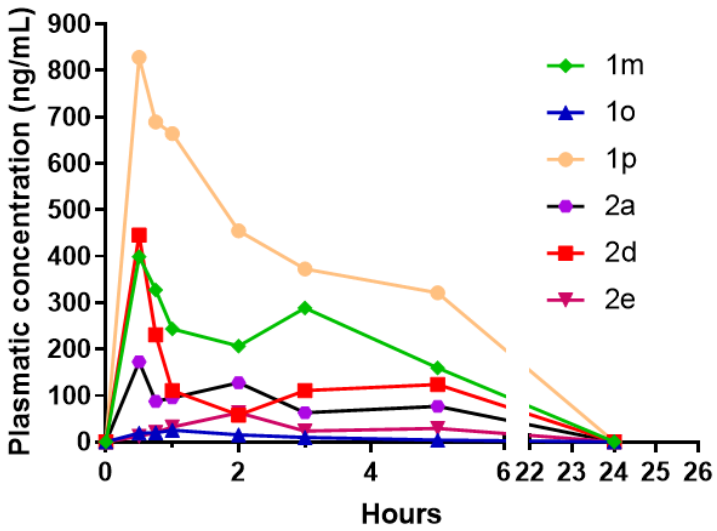

Figure 11. Absolute plasma concentrations (ng/mL) for compounds **1m**, **1o**, **1p**, **2a**, **2d**, **2e** determined in SNAP-PK studies on BALB/c mice after oral administration of 20 mg/kg dose complex with cyclodextrin.

Table 4. Pharmacokinetic parameters of compounds **1m**, **1o-p**, **2a**, **2d-e.**

Compound	Dose (mg/kg)	C_{max} (ng/mL)	C_{max} (µM)	T_{max} (h)	AUC_{last} (ng/mL*h)	AUC_{last} (nM*h)	$T_{½}$ (h)
1m	20	399	1.3	0.5	2703	8490.8	2.1
1o	20	25	0.1	1	107	323.3	4.5
1p	20	828	2.5	1	5291	16013.2	2.1
2a	20	373	0.4	0.5	1180	1183	3.0
2d	20	446	1.1	0.5	1818	4328.5	2.4
2e	20	63	0.1	2	435	967.1	3.0

Before proceeding to *in vivo* studies on infected mice, the capability of **1p** and **2e** to achieve plasma concentrations consistent with parasite elimination was evaluated. To evaluate the anti-parasitic potential of the detected plasma concentrations, expressed in µM, these were normalized to the *T. brucei* anti-parasitic activity by dividing the concentration detected in each time points by the EC_{50} of the respective compound. These normalized pharmacokinetic profiles are shown in **Figure 12**. Values >1 indicate that plasma concentrations are higher than the anti-parasitic EC_{50} and therefore the tested compounds should be able to kill the bloodstream form of *T. brucei*. Compound **2e** showed a normalized pharmacokinetic profile <1 in the 24 h, thus its plasma concentration is not expected to

be sufficient for parasite elimination; whilst **1p** reached in the same conditions a 28-fold higher plasmatic concentration than its anti-*T. brucei* EC_{50} and kept it above the 10-fold in the first 5 h after administration. Notwithstanding the molecule presents a swift elimination, after 24 hours it was undetectable. This was a concern because the molecule must be maintained at a high level for a sufficient time span to be effective, the date presented a rather short time window. Therefore, considering the promising biological and pharmacokinetic profile, **1p** was deemed suitable for *in vivo* tests in infected mice.

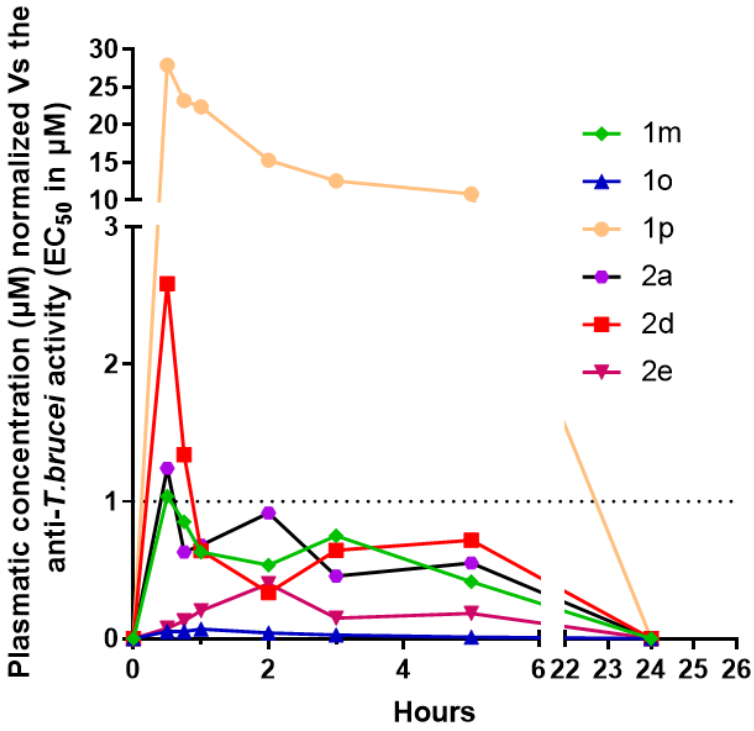

Figure 12. Plasma concentration detected for compounds **1m**, **1o-p**, **2a**, **2d-e**, determined in Snap-PK studies on BALB/c mice after oral administration of 20mg/Kg of 20 mg/kg dose complex with cyclodextrin, normalized for anti-*T. brucei* activity (EC_{50} in µM). This is calculated by dividing the concentration detected in each time points by the EC_{50} of the respective compound. The dashed line represents when the concentration in the blood is equal to the EC_{50}.

Considering the **1p** optimal anti-trypanosomal activity, *in vitro* inhibition of *Tb*PTR1, toxicity and promising pharmacokinetic profile for oral administration, we performed an *in vivo* anti-parasitic evaluation using a BALB/c *T. brucei* model of infection. The experimental setup was bi-daily administration of 20 mg/kg of 1p in a 50% cyclodextrin suspension. In these conditions, **1p** was not capable of controlling infection with similar parasitemia and survival to untreated controls.

Intraperitoneal pentamidine at 5mg/kg/day fully cleared infection (data not shown). The lack of activity in murine models of infection might be related to the fast elimination of **1p**. This might result in a rapid decrease of the compounds concentrations for the time lapse required to be anti-parasitic. Considering the possible compound mechanism of action associated with PTR1 inhibition, this might require a constant high concentration of **1p** to maintain a sustainable biological activity.

Conclusions

In the present work, the activity of differently substituted nitroalkylpyrimidine, was investigated towards the parasitic pteridine reductase 1 (PTR1) of both *T. brucei* and *L. infantum*. The starting compounds were active against the parasites but without sufficient activity towards the target protein. Basing our design on the 5 nitroethyl-pyrimidine we were able to obtain 23 compounds showing low nanomolar efficacy against the PTR1 protein. The addition of one single aromatic ring infers higher affinity (10 folds) than fused double rings heterocycles and phenoxy derivatives. PTR1 enzyme can allocate the tested compounds in its active site where the **TAP** fragment binds (orthosteric site). The different fragments cause small difference in the binding geometries, sometimes allocating them towards the S1 hydrophobic cavity (aromatic ring). While the nitro-ethyl is located in S2 sub-pocket. We have demonstrated that the synthesized library of compounds is active on low micromolar to high nanomolar activity on parasitic cell lines. Their structure relationships activities were better investigated with computational strategies, that evidenced that, despite the different binding mode of the heterocyclic substituent, their inhibitory activity is predominantly exerted by the pyrimidine core.

The compound showing the best pharmacokinetic activity is **1p**, that also displays an EC_{50} (*T. brucei*) of 0.09 μM and an IC_{50} of 0.3 μM on the recombinant *Tb*PTR1. If we directly compare the plasma concentration of **1p** and **2d** with their respective EC_{50} (*T. brucei*) (Figure 1), it emerges that both compounds **1p** and **2d** reach respectively 30 and 2.5-fold the parasitic EC_{50}, being good candidates for in vitro administration and retaining their trypanocidal activity. In particular, **1p** maintains a plasma concentration 10-30 fold higher than its predicted anti-*T. brucei* activity $IC_{50(T.\ brucei)}$ during the 5 hours after its administration, and will be employed in the next studies to test the antiparasitic activity against *T.brucei* infected mice. Finally, the toxicity of all compounds was investigated by measuring the inhibitory effect on the *h*ERG ion-channel (cardiotoxicity), inhibition of representative cytochrome P450 isoforms (hepatotoxicity), mitochondrial toxicity, and for cytotoxicity against A549 human lung carcinoma cells. If compared to their EC_{50}, these studies evidence that **1p** and **2e** display up to 100 selectivity towards their targets with toxicity compared to that of the reference

compounds miltefosine and pentamidine. Despite containing a nitrobenzene moiety, our compounds **1p** and **2e** do not display cardiotoxicity and hepatotoxicity on in vitro preliminary tests, suggesting that they may not be metabolized by human reductases. Overall, the enhancement of properties of compounds **1p** and **2e** are summarized in Figure 13, that displays the improvement of the activity on target, in vitro and on the animal model expressed as direct **1p**/**2e.** Despite they both represent a good starting point for the development of new antiparasitic agent for their *on target* and *in vitro* properties, compound **1p** displays better *in vivo* properties compared to **2e**, with 15-fold increase in its plasma concentration expressed as AUC, and 100-fold increase in its plasma concentration normalized to EC_{50} on *Tb*.

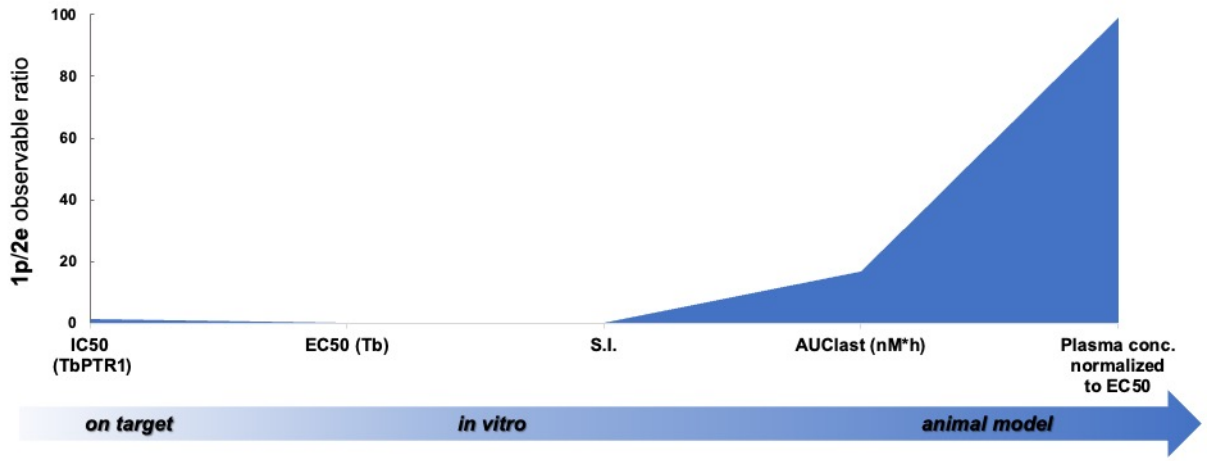

Figure 13. Graphical representation of the biological properties' variations for compounds **1p** and **2e**. On the x-axis the observable data ratio for **1p** and **2a** are reported regarding IC_{50} against *Tb*PTR1, EC_{50} against *Tb*, Selectivity Index (SI), AUC and Plasma concentration normalized to EC_{50}. This latest parameter is obtained by dividing the maximum plasma concentration of **1p** and **2e** by their calculated EC_{50} against *Tb*, as reported in Figure 12. Numerical values employed to build this trendline are reported in Table S5, Supplementary Information.

The nitro group moiety present in the active compound **1p**, can be important for its toxicity. However the presence of higher concentration of nitroreductases (NTRs) in parasite cytosolic environment which are able to metabolize the nitro group containing drugs such as nifurtimox and benznidazole before they develop human cytotoxicity [33,34], may leverage the expected effect. In the next step

experiments, *in vivo* activity will reveal the occurrence of an accountable nitro reduction to hydroxylamine and to aniline, and if this conversion determines a partial loss of trypanocidal activity. Overall, in this paper we demonstrate that nitroalkylpyrimidine is a suitable chemical scaffold for the development of anti-parasitic molecules with both good on target activity and adequate *in vivo* PK properties. Our docking poses and SAR analyses provide the basis for the rationale design of more potent and selective derivatives with improved selectivity and longer *in vivo* half-life, able to overcome the issues of the currently marketed drugs for trypanosomiases and leishmaniases.

Experimental section

Synthetic procedures

All commercially available chemicals and solvents were reagent grade and were used without further purification unless otherwise specified. Reactions were monitored by thin-layer chromatography on silica gel plates (60F-254, E. Merck) and visualized with UV light, iodine vapors, cerium ammonium sulphate or alkaline $KMnO_4$ aqueous solution. The following solvents and reagents have been abbreviated: ethyl ether (Et_2O), dimethyl sulfoxide (DMSO), ethyl acetate (EtOAc), dichloromethane (DCM), methanol (MeOH). All reactions were carried out with standard techniques or under microwave irradiation. NMR spectra were recorded on a Bruker 400 spectrometer with 1H at 400.134 MHz and 13C at 100.62 MHz. Proton chemical shift was referenced to the residual solvent peak. Chemical shifts are reported in parts per million (ppm, δ units). Coupling constants are reported in units of Hertz (Hz). Splitting patterns are designated as s, singlet; d, doublet; t, triplet; q quartet; dd, double doublet; m, multiplet; b, broad. Mass spectra were obtained on a 6520 Accurate-Mass Q-TOF LC/MS and 6310A Ion TrapLC-MS(n). The melting point was recorded on a Stuart, SMP3 (Barloworld Scientific Limited Stone, Staffordshire, UK) and was uncorrected.

General procedure for the synthesis of aryl-2-nitroethyl pyrimidines 1a-q and 2a-e

To a solution of nitro-styrene (1 eq.) in AcOEt (10 mL), 2,4,6-triaminopyrimidine (1 eq.) solubilized in an equal volume of water was added at room temperature. The biphasic mixture was stirred under vigorous agitation at 60 °C. After 18 h the mixture was chilled at room temperature and the organic phase separated. The latter was washed with water, NaCl saturated solution, dried over anhydrous $NaSO_4$ and concentrated. The crude material was crystalized from diethyl ether and filtered to give the pure desired product, without any further purification.

5-(1-(4-chlorophenyl)-2-nitroethyl)pyrimidine-2,4,6-triamine (1a)

White solid. 67% yield. ^{1}H NMR (400 MHz, DMSO-d6) δ 5.00 (t, J = 7.9 Hz, 1H), 5.10 (dd, J = 8.9, 13.2 Hz, 1H), 5.30 – 5.50 (m, 7H), 7.10 – 7.22 (m, 2H), 7.42 – 7.55 (m, 2H). ^{13}C NMR (101 MHz, DMSO) δ 36.70, 75.48, 83.69, 119.23, 129.87, 131.01, 138.20, 161.33, 162.19. HRMS m/z $[M+H]^+$ calcd. for $C_{12}H_{14}ClN_6O_2$: 309.0861, found: 309.0855. m.p. [127 °C with dec.].

5-(1-(3,4-dichlorophenyl)-2-nitroethyl)pyrimidine-2,4,6-triamine (1b)

White solid. 53% yield. ^{1}H NMR (400 MHz, DMSO-d6) δ 5.04 (t, J = 7.8 Hz, 1H), 5.17 (dd, J = 9.0, 13.4 Hz, 1H), 5.40 – 5.65 (m, 7H), 7.22 (dd, J = 2.2, 8.5 Hz, 1H), 7.48 (d, J = 2.2 Hz, 1H), 7.59 (d, J = 8.5 Hz, 1H). ^{13}C NMR (101 MHz, DMSO) δ 36.76, 73.86, 75.21, 82.97, 127.63, 129.07, 130.29, 130.83, 140.22, 160.90, 162.04. HRMS m/z $[M+H]^+$ calcd. for $C_{12}H_{13}Cl_2N_6O_2$: 343.0472, found: 343.0470. m.p. [165 °C with dec.].

5-(1-(4-bromophenyl)-2-nitroethyl)pyrimidine-2,4,6-triamine (1c)

Pale yellow solid. 46% yield. ^{1}H NMR (400 MHz, DMSO-d_6) δ 5.01 (t, J = 7.9 Hz, 1H), 5.15 (dd, J = 8.9, 13.2 Hz, 1H), 5.34 – 5.59 (m, 7H), 7.14 – 7.26 (m, 2H), 7.47 – 7.57 (m, 2H). ^{13}C NMR (101 MHz, DMSO) δ 36.95, 75.34, 83.77, 119.57, 129.25, 131.11, 138.64, 161.25, 162.26. HRMS m/z $[M+H]^+$ calcd. for $C_{12}H_{14}BrN_6O_2$: 353.0356, found: 353.0350. m.p. [138 °C with dec.].

5-(1-(3-bromophenyl)-2-nitroethyl)pyrimidine-2,4,6-triamine (1d)

Pale yellow solid. 59% yield. ^{1}H NMR (400 MHz, DMSO-*d*6) δ 5.04 (t, J = 7.9 Hz, 1H), 5.17 (dd, J = 8.9, 13.2 Hz, 1H), 5.43 (s, 2H), 5.46 – 5.65 (m, 5H), 7.28 – 7.32 (m, 2H), 7.43 – 7.45 (m, 2H). ^{13}C NMR (101 MHz, DMSO) δ 37.13, 75.32, 83.56, 121.77, 126.00, 129.40, 129.83, 130.37, 142.08, 161.29, 162.26. HRMS m/z $[M+H]^+$ calcd. for $C_{12}H_{14}BrN_6O_2$: 353.0356, found: 353.0355. m.p. [132 °C with dec.].

5-(1-(3-nitrophenyl)-2-nitroethyl)pyrimidine-2,4,6-triamine (1e)

Yellow solid. 41% yield. ^{1}H NMR (400 MHz, DMSO-d_6) δ 5.21 (ddd, J = 8.7, 14.0, 22.6 Hz, 2H), 5.51 (s, 2H), 5.63 (q, J = 5.8, 6.3 Hz, 5H), 7.64 (t, J = 7.9 Hz, 1H), 7.72 (d, J = 8.1 Hz, 1H), 8.04 – 8.16 (m, 2H). ^{13}C NMR (101 MHz, DMSO) δ 37.19, 75.34, 83.04, 121.56, 121.90, 129.66, 133.98, 141.51, 147.77, 161.02, 162.13. HRMS m/z $[M+H]^+$ calcd. for $C_{12}H_{14}N_7O_4$: 320.2885, found: 320.2881. m.p. [152 °C with dec.].

5-(1-(3,4-dimethoxyphenyl)-2-nitroethyl)pyrimidine-2,4,6-triamine (1f)

White solid. 57% yield. ^{1}H NMR (400 MHz, DMSO-d_6) δ 3.71 (s, 3H), 3.73 (s, 3H), 4.97 (t, J = 7.9 Hz, 1H), 5.12 (dd, J = 9.0, 12.9 Hz, 1H), 5.30 – 5.50 (m, 7H), 6.78 (dd, J = 2.1, 8.4 Hz, 1H), 6.84 (d,

J = 2.1 Hz, 1H), 6.90 (d, *J* = 8.3 Hz, 1H). ^{13}C NMR (101 MHz, DMSO) δ 37.10, 55.48, 55.50, 75.65, 84.50, 111.26, 111.67, 118.50, 131.36, 147.59, 148.72, 161.19, 162.33. HRMS m/z $[M+H]^+$ calcd. for $C_{14}H_{19}N_6O_4$: 335.1462, found: 335.1460. m.p. [180 °C with dec.].

2-methoxy-4-(2-nitro-1-(2,4,6-triaminopyrimidin-5-yl)ethyl)phenol (1g)

White solid. 40% yield. ^{1}H NMR (400 MHz, DMSO-*d*$_6$) δ 3.73 (s, 3H), 4.93 (t, *J* = 7.9 Hz, 1H), 5.09 (dd, *J* = 9.1, 12.9 Hz, 1H), 5.31 – 5.42 (m, 7H), 6.65 (dd, *J* = 2.2, 8.4 Hz, 1H), 6.72 (d, *J* = 8.2 Hz, 1H), 6.81 (d, *J* = 2.1 Hz, 1H). ^{13}C NMR (101 MHz, DMSO) δ 37.03, 55.66, 64.87, 75.70, 84.71, 111.53, 115.32, 118.85, 129.65, 145.32, 147.60, 162.28. HRMS m/z $[M+H]^+$ calcd. for $C_{13}H_{17}N_6O_4$: 321.1306, found: 321.1305. m.p. [168 °C with dec.].

5-(1-(2,6-dimethoxyphenyl)-2-nitroethyl)pyrimidine-2,4,6-triamine (1h)

White solid. 70% yield. ^{1}H NMR (400 MHz, DMSO-*d*$_6$) δ 3.78 (s, 6H), 4.92 (dd, *J* = 7.6, 13.3 Hz, 1H), 5.02 (t, *J* = 8.0 Hz, 1H), 5.18 (dd, *J* = 8.4, 13.3 Hz, 1H), 5.31 (s, 2H), 5.48 (s, 4H), 6.71 (d, *J* = 8.4 Hz, 2H), 7.23 (t, *J* = 8.3 Hz, 1H). ^{13}C NMR (101 MHz, DMSO) δ 31.11, 55.78, 75.73, 84.36, 104.82, 114.50, 128.22, 157.46, 160.81, 162.15. HRMS m/z $[M+H]^+$ calcd. for $C_{14}H_{19}N_6O_4$: 335.1462, found: 335.1465. m.p. [154 °C with dec.].

5-(1-(furan-2-yl)-2-nitroethyl)pyrimidine-2,4,6-triamine (1i)

White solid. 48% yield. ^{1}H NMR (400 MHz, DMSO-*d*$_6$) δ 5.04 (q, *J* = 4.1, 5.8 Hz, 2H), 5.27 (d, *J* = 4.8 Hz, 1H), 5.43 (s, 2H), 5.51 (s, 4H), 6.28 (d, *J* = 3.3 Hz, 1H), 6.37 – 6.49 (m, 1H), 7.60 (s, 1H). ^{13}C NMR (101 MHz, DMSO) δ 33.23, 74.54, 81.74, 106.42, 110.35, 142.31, 152.08, 161.19, 162.26. HRMS m/z [M+H]+ calcd. for $C_{10}H_{13}N_6O_3$: 265.1044, found: 265.1045, m. p. [149°C with dec.].

5-(2-nitro-1-(thiophen-2-yl)ethyl)pyrimidine-2,4,6-triamine (1j)

Pale brown solid. 41% yield. 1H NMR (400 MHz, DMSO-d6) δ 5.08 – 5.27 (m, 2H), 5.36 – 5.45 (m, 1H), 5.52 (s, 6H), 6.94 – 7.04 (m, 2H), 7.43 (dd, J = 1.3, 5.0 Hz, 1H). 13C NMR (101 MHz, DMSO) δ 34.31, 75.81, 84.31, 123.91, 125.20, 126.66, 143.72, 160.86, 161.92. HRMS m/z [M+H]+ calcd. for $C_{10}H_{13}N_6O_2S$: 281.0815, found: 281.0815, m. p. [135°C with dec.].

5-(1-(5-methylthiophen-2-yl)-2-nitroethyl)pyrimidine-2,4,6-triamine (1k)

Pale brown solid. 46% yield. ^{1}H NMR (400 MHz, DMSO-*d*$_6$) δ 2.09 (s, 3H), 5.11 (d, *J* = 5.7 Hz, 2H), 5.40 (d, *J* = 46.0 Hz, 7H), 6.07 (s, 1H), 6.63 (d, *J* = 3.4 Hz, 1H), 6.76 (d, *J* = 3.5 Hz, 1H). Signals in the ^{13}C spectra were not detected due to the high insolubility of the compound. HRMS m/z [M+H]+ calcd. for $C_{11}H_{15}N_6O_2S$: 295.0972, found: 295.0975, m. p. [142 °C with dec.].

5-(1-(benzo[d][1,3]dioxol-5-yl)-2-nitroethyl)pyrimidine-2,4,6-triamine (1l)

White solid. 67% yield. ^{1}H NMR (400 MHz, DMSO-d_6) δ 4.94 (dd, J = 7.0, 8.9 Hz, 1H), 5.11 (dd, J = 8.9, 13.1 Hz, 1H), 5.38 (m, 7H), 5.95 – 6.02 (m, 2H), 6.73 (dd, J = 1.8, 8.1 Hz, 1H), 6.80 (d, J = 1.7 Hz, 1H), 6.86 (d, J = 8.1 Hz, 1H). ^{13}C NMR (101 MHz, DMSO) δ 37.15, 75.60, 100.93, 107.67, 107.95, 119.48, 132.99, 145.82, 147.42, 161.22, 162.26. HRMS m/z [M+H]+ calcd. for $C_{13}H_{15}N_6O_4$: 319.1149, found: 319.1150, m. p. [147 °C with dec.].

5-(1-(benzo[d][1,3]dioxol-4-yl)-2-nitroethyl)pyrimidine-2,4,6-triamine (1m)

White solid. 58% yield. ^{1}H NMR (400 MHz, DMSO-d_6) δ 4.94 – 5.18 (m, 2H), 5.36 (dd, J = 6.9, 13.3 Hz, 1H), 5.41 (s, 2H), 5.48 (s, 4H), 6.00 (d, J = 2.0 Hz, 2H), 6.71 (dd, J = 1.6, 7.6 Hz, 1H), 6.77 – 6.90 (m, 2H). ^{13}C NMR (101 MHz, DMSO) δ 34.41, 74.25, 82.62, 100.58, 107.26, 120.38, 120.88, 121.73, 144.62, 147.06, 161.27, 162.27. HRMS m/z [M+H]+ calcd. for $C_{13}H_{15}N_6O_4$: 319.1149, found: 319.1150, m. p. [dec. 150 °C].

5-(1-(2,3-dihydrobenzofuran-5-yl)-2-nitroethyl)pyrimidine-2,4,6-triamine (1n)

White solid. 63% yield. 1H NMR (400 MHz, DMSO-d6) δ 3.14 (t, J = 8.7 Hz, 2H), 4.50 (t, J = 8.7 Hz, 2H), 4.95 (t, J = 7.9 Hz, 1H), 5.10 (dd, J = 9.0, 12.9 Hz, 1H), 5.37 (m, 7H), 6.71 (d, J = 8.3 Hz, 1H), 6.98 (dd, J = 2.1, 8.3 Hz, 1H), 7.10 (d, J = 1.9 Hz, 1H). ^{13}C NMR (101 MHz, DMSO) δ 29.06, 36.77, 70.89, 75.69, 84.90, 108.49, 123.74, 125.86, 127.62, 130.86, 161.17, 162.15, 162.25. HRMS m/z [M+H]+ calcd. for $C_{14}H_{17}N_6O_3$: 317.1357, found: 317.1360, m. p. [dec. 140°C].

5-(1-(2,3-dihydrobenzo[b][1,4]dioxin-6-yl)-2-nitroethyl)pyrimidine-2,4,6-triamine (1o)

White solid. 51% yield. ^{1}H NMR (400 MHz, DMSO-d_6) δ 4.21 (s, 4H), 4.92 (t, J = 7.9 Hz, 1H), 5.11 (dd, J = 8.9, 13.0 Hz, 1H), 5.39 (dd, J = 6.9, 13.0 Hz, 1H), 5.51 (d, J = 18.4 Hz, 5H), 6.60 – 6.88 (m, 3H). ^{13}C NMR (101 MHz, DMSO) δ 36.77, 63.99, 64.07, 75.63, 84.30, 115.60, 116.88, 119.53, 131.95, 142.02, 143.17, 161.17, 162.28. HRMS m/z $[M+H]^+$ calcd. for $C_{14}H_{17}N_6O_4$: 333.1306, found: 333.1305, m. p. [139 °C with dec.].

5-(1-(benzo[b]thiophen-3-yl)-2-nitroethyl)pyrimidine-2,4,6-triamine (1p)

Pale yellow solid. 48% yield.^{1}H NMR (400 MHz, DMSO-d_6) δ 5.12 – 5.27 (m, 2H), 5.34 (s, 2H), 5.47 – 5.54 (m, 5H), 7.35 (pd, J = 1.5, 7.1 Hz, 2H), 7.75 (ddd, J = 1.4, 3.1, 4.6 Hz, 2H), 7.96 – 8.00 (m, 1H). ^{13}C NMR (101 MHz, DMSO) δ 33.80, 75.03, 82.61, 121.54, 122.60, 122.78, 124.01, 124.68, 134.42, 138.09, 139.53, 161.08, 162.22. HRMS m/z $[M+H]^+$ calcd. for $C_{14}H_{15}N_6O_2S$: 331.0972, found: 331.0972, m. p. [153 °C with dec.].

5-(1-(1H-indol-3-yl)-2-nitroethyl)pyrimidine-2,4,6-triamine (1q)

Orange solid. 40% yield.^{1}H NMR (400 MHz, DMSO-d_6) δ 5.08 – 5.25 (m, 2H), 5.30 – 5.44 (m, 3H), 5.45 – 5.60 (m, 4H), 6.84 – 6.96 (m, 1H), 7.08 (ddd, J = 1.1, 7.0, 8.3 Hz, 1H), 7.31 – 7.41 (m, 4H), 11.00 (d, J = 2.4 Hz, 1H). ^{13}C NMR (101 MHz, DMSO) δ 31.32, 64.87, 75.55, 83.83, 111.36, 112.57, 118.37, 119.39, 121.32, 121.55, 126.20, 136.57, 160.65, 162.04. HRMS m/z [M+H]+ calcd. for $C_{14}H_{16}N_7O_2$: 314.1360, found: 314.1362, m. p. [163 °C with dec.].

5-(1-(2-((3,4-dichlorobenzyl)oxy)phenyl)-2-nitroethyl)pyrimidine-2,4,6-triamine (2a)

Pale yellow solid. 65% yield.^{1}H NMR (400 MHz, DMSO-d_6) δ 4.98 – 5.10 (m, 2H), 5.16 (s, 2H), 5.28 – 5.43 (m, 7H), 6.94 (td, J = 1.1, 7.5 Hz, 1H), 7.03 (dd, J = 1.1, 8.4 Hz, 1H), 7.23 (ddd, J = 1.6, 7.4, 8.8 Hz, 1H), 7.31 (dd, J = 1.6, 7.7 Hz, 1H), 7.38 (dd, J = 2.0, 8.3 Hz, 1H), 7.59 (d, J = 8.3 Hz, 1H), 7.72 (d, J = 2.0 Hz, 1H). ^{13}C NMR (101 MHz, DMSO) δ 36.68, 67.71, 74.83, 83.70, 112.42, 120.64, 127.03, 127.56, 127.60, 128.00, 128.07, 129.28, 130.15, 130.42, 131.00, 133.91, 138.11, 155.51, 161.12, 162.23. $C_{19}H_{19}[^{35}Cl]_2N_6O_3$: 449.0890, found: 449.0890; calcd. for $C_{19}H_{19}[^{35}Cl][^{37}Cl]N_6O_3$: 451.0861, found: 451.0862, m. p. [130°C with dec.]

5-(1-(2-(benzyloxy)phenyl)-2-nitroethyl)pyrimidine-2,4,6-triamine (2b)

Pale yellow solid. 72% yield.^{1}H NMR (400 MHz, DMSO-d_6) δ 4.98 – 5.10 (m, 2H), 5.17 (s, 2H), 5.33 (d, J = 5.1 Hz, 7H), 6.92 (td, J = 1.1, 7.5 Hz, 1H), 7.06 (dd, J = 1.1, 8.3 Hz, 1H), 7.22 (ddd, J = 1.6, 7.4, 8.9 Hz, 1H), 7.27 – 7.34 (m, 2H), 7.34 – 7.40 (m, 2H), 7.40 – 7.50 (m, 2H). ^{13}C NMR (101 MHz, DMSO) δ 34.42, 69.36, 74.89, 83.89, 112.55, 120.48, 126.87, 127.41, 127.66, 127.83, 128.05, 128.32, 136.81, 155.80, 161.15, 162.28, 164.44. HRMS m/z [M+H]+ calcd. for $C_{19}H_{21}N_6O_3$: 381.1670, found: 381.1665, m. p. [127°C with dec.].

5-(2-nitro-1-(2-((2-nitrobenzyl)oxy)phenyl)ethyl)pyrimidine-2,4,6-triamine (2c)

Pale yellow solid. 59% yield.^{1}H NMR (400 MHz, DMSO-d_6) δ 5.08 (d, J = 9.0 Hz, 2H), 5.31 – 5.50 (m, 7H), 5.53 (s, 2H), 6.97 (dd, J = 6.9, 8.0 Hz, 1H), 7.02 (d, J = 8.1 Hz, 1H), 7.23 (td, J = 1.6, 7.4, 7.9 Hz, 1H), 7.34 (dd, J = 1.6, 7.8 Hz, 1H), 7.60 (ddd, J = 1.9, 7.0, 8.7 Hz, 1H), 7.69 (dq, J = 7.1, 8.6 Hz, 2H), 8.17 (dd, J = 1.3, 8.1 Hz, 1H). Signals in the ^{13}C spectra were not detected due to the high insolubility of the compound. HRMS m/z [M+H]+ calcd. for $C_{19}H_{20}N_7O_5$: 426.1520, found: 426.1515, m. p. [154°C with dec.].

5-(1-(2-((3-chlorobenzyl)oxy)phenyl)-2-nitroethyl)pyrimidine-2,4,6-triamine (2d)

Pale yellow solid. 72% yield.^{1}H NMR (400 MHz, DMSO-d_6) δ 5.02 – 5.13 (m, 2H), 5.18 (d, J = 1.9 Hz, 2H), 5.28 – 5.47 (m, 7H), 6.94 (t, J = 7.4 Hz, 1H), 7.03 (d, J = 8.1 Hz, 1H), 7.23 (td, J = 1.6, 7.8 Hz, 1H), 7.30 (dd, J = 1.6, 7.7 Hz, 1H), 7.37 (t, J = 1.8 Hz, 3H), 7.54 (d, J = 2.1 Hz, 1H). ^{13}C NMR (101 MHz, DMSO) δ 34.36, 68.44, 74.92, 83.70, 112.48, 120.61, 125.87, 126.93, 127.05, 127.59, 127.76, 128.09, 130.19, 133.06, 139.47, 155.65, 161.18, 162.30. HRMS m/z [M+H]+ calcd. for $C_{19}H_{20}ClN_6O_3$: 415.1280, found: 415.1281, m. p. [161°C with dec.].

5-(1-(4-((3,4-dichlorobenzyl)oxy)phenyl)-2-nitroethyl)pyrimidine-2,4,6-triamine (2e)

^{1}H NMR (400 MHz, DMSO-d_6) δ 4.96 – 4.99 (m, 1H), 5.09 – 5.13 (m, 3H), 5.36 – 5.42 (m, 7H), 6.97 (d, J = 7.4 Hz, 2H), 7.18 (d, J = 7.4 Hz, 2H), 7.45 (d, J = 6.8 Hz, 1H), 7.66 (d, J = 6.8 Hz, 1H), 7.72 (s, 1H). ^{13}C NMR (101 MHz, DMSO) δ 36.68, 67.57, 75.59, 84.56, 114.72, 115.55, 127.74, 127.97, 129.38, 130.26, 130.64, 131.04, 131.49, 138.37, 156.56, 161.16, 162.25. HRMS m/z [M+H]+ calcd. for $C_{19}H_{19}[^{35}Cl]_2N_6O_3$: 449.0890, found: 449.0887; calcd. for $C_{19}H_{19}[^{35}Cl][^{37}Cl]N_6O_3$: 451.0861, found: 451.0860, m. p. [89°C with dec.].

General procedure for the synthesis of (*E*)-(2-nitrovinyl)arene (3a-q, 4a-e)

To a solution of the appropriate aldehyde (1 equiv.) in nitromethane, NH4AcO (1.5 equiv.) was added and the solution was refluxed for 6-7 hours. Upon cooling, a bright yellow solid crystalized, which was collected by filtration. The solid was recrystallized from methanol to give the titled compound (as *E*-isomer) as a bright yellow/orange solid.

(E)-1-chloro-4-(2-nitrovinyl)benzene (3a)

Yellow solid. 45% yield. ^{1}H NMR (400 MHz, $CDCl_3$): δ 7.98 (d, J = 13.7 Hz, 1H), 7.58 (d, J = 13.7 Hz, 1H), 4.12 – 3.59 (m, 4H), 7.54-42 (m, 4H).

(E)-1,2-dichloro-4-(2-nitrovinyl)benzene (3b)

Yellow solid. 55% yield. ^{1}H NMR (400 MHz, $CDCl_3$): δ = 7.37-7.39 (1H, dd, J = 8.3 Hz and J = 2.0 Hz), 7.54 (1H, d, J = 13.6 Hz), 7.55 (1H, s), 7.6 (1H, d, J = 2.0 Hz), 7.90 (1H, d, J = 13.6 Hz).

(E)-1-bromo-4-(2-nitrovinyl)benzene (3c)

Yellow solid. 38% yield. ^{1}H NMR (400 MHz, $CDCl_3$): δ 7.98 (d, J = 13.7 Hz, 1H), 7.62 (m, 3H), 7.45 (d, 8.5 Hz, 2H).

(E)-1-bromo-3-(2-nitrovinyl)benzene (3d)

Yellow solid. 42% yield. ^{1}H NMR (400 MHz, $CDCl_3$): δ 7.87 (d, J = 13.7 Hz, 1H), 7.64 (t, J = 1.6 Hz, 1H), 7.57 (d, J = 7.8 Hz, 1H), 7.55 (d, J = 13.7 Hz, 1H), 7.47 (d, J = 7.8 Hz, 1H), 7.31 (t, J = 7.9 Hz, 1H).

(E)-1-nitro-3-(2-nitrovinyl)benzene (3e)

Pale yellow solid. 78% yield. ^{1}H NMR (400 MHz, $CDCl_3$): δ 8.42 (t, J = 1.8 Hz, 1H), 8.35 (ddd, J = 8.1, 1.8, 1.2 Hz, 1H), 8.05 (d, J = 13.5 Hz, 1H), 7.87 (dt, J = 7.5, 1.2 Hz, 1H), 7.68 (t, J = 7.8 Hz, 1H), 7.66 (d, J = 13.8 Hz, 1H).

(E)-1,2-dimethoxy-4-(2-nitrovinyl)benzene (3f)

Pale yellow solid. 90% yield. ^{1}H NMR (400 MHz, $CDCl_3$): δ 7.97 (d, J = 13.5 Hz, 1H), 7.53 (d, J = 13.5 Hz, 1H), 7.18 (dd, J = 8.7, 2.1 Hz, 1H), 7.01 (d, J = 2.1 Hz, 1H), 6.92 (d, J = 8.7 Hz, 1H), 3.94 (s, 3H), 3.93 (s, 3H).

(E)-2-methoxy-4-(2-nitrovinyl)phenol (3g)

Pale yellow solid. 61% yield. ^{1}H NMR (400 MHz, DMSO-d_6): δ 10.00 (s, 1H), 8.13 (d, J = 13.4 Hz, 1H), 8.01 (d, J = 13.4 Hz, 1H), 7.46 (s, 1H), 7.28 (d, J = 8.2Hz, 1H), 6.84 (d, J = 8.2 Hz, 1H), 3.81 (d, J = 5.4 Hz, 3H).

(E)-1,3-dimethoxy-2-(2-nitrovinyl)benzene (3h)

Pale yellow solid. 70% yield. ^{1}H NMR (400 MHz, $CDCl_3$): δ 8.55 (d, J = 13.6 Hz, 1H), 8.07 (d, J = 13.6 Hz, 1H), 7.38 (t, J = 8.4 Hz, 1H), 6.58 (d, J = 8.5 Hz, 2H), 3.93 (s, 6H);

(E)-2-(2-nitrovinyl)furan (3i)

Pale brown solid. 35% yield. ^{1}H NMR (400 MHz, $CDCl_3$): δ 7.75 (d, J = 13.2 Hz, 1H), 7.56 (d, J = 1.4 Hz, 1H), 7.50 (d, J = 13.2 Hz, 1H), 6.86 (d, J = 3.5 Hz, 1H), 6.55 (dd, J = 3.5, 1.8 Hz, 1H).

(E)-2-(2-nitrovinyl)thiophene (3j)

Orange solid. 43% yield. ^{1}H NMR (400 MHz, $CDCl_3$): δ 7.13 – 7.18 (dd, J = 5.1, 3.7 Hz, 1H), 7.45 – 7.48 (m, 2H), 7.49 – 7.52 (s, 1H), 7.55 – 7.59 (dt, J = 5.0, 1.0, 1.0 Hz, 1H), 8.13 – 8.19 (d, J = 13.4, 1H).

(E)-2-methyl-5-(2-nitrovinyl)thiophene (3k)

Orange solid. 31% yield. ^{1}H NMR (400 MHz, DMSO-d_6): δ 8.28 (d, J= 13.2 Hz, 1H),7.84 (d, J= 13.2 Hz, 1H), 7.65 (d, J= 4.2 Hz, 1H), 6.97(d, J= 4.2 Hz, 1H), 2.52 (s, 3H).

(E)-5-(2-nitrovinyl)benzo[d][1,3]dioxole (3l)

Orange solid. 84% yield. ^{1}H NMR (400 MHz, $CDCl_3$) δ 6.06 (s, 2H), 6.79 – 7.12 (m, 3H), 7.42 – 7.51 (d, J = 13.6 Hz, 1H), 7.87 – 7.96 (d, J = 13.6 Hz, 1H).

(E)-4-(2-nitrovinyl)benzo[d][1,3]dioxole (3m)

Orange solid. 69% yield. ^{1}H NMR (400 MHz, $CDCl_3$) δ 6.14 (s, 2H), 6.95 (m, 3H), 7.84 (d, J 13.6 Hz, 1H), 7.93 (d, J 14.2 Hz, 1H).

(E)-5-(2-nitrovinyl)-2,3-dihydrobenzofuran (3n)

Orange solid. 75% yield. ^{1}H NMR (400 MHz, $CDCl_3$) δ 3.23 (t, J = 7.1 Hz, 1H), 4.54 (t, J = 7.1 Hz, 1H), 6.89 (d, J = 7.5 Hz, 0H), 7.29 (d, J = 7.5 Hz, 0H), 7.46 (s, 0H), 7.94 (q, J = 15.1 Hz, 1H).

(E)-6-(2-nitrovinyl)-2,3-dihydrobenzo[b][1,4]dioxine (3o)

Yellow solid. 84% yield. ^{1}H NMR (400 MHz, $CDCl_3$) δ 4.30 (s, 4H), 6.91 (d, J = 6.0 Hz, 1H), 7.05 (dd, J = 3.0 Hz, J = 6.0 Hz, 1H), 7.07 (d, J = 3.0 Hz, 1H), 7.47 (d, J = 13.5 Hz, 1H), 7.90 (d, J = 13.5 Hz, 1H).

(E)-3-(2-nitrovinyl)benzo[b]thiophene (3p)

Yellow solid. 64% yield. ^{1}H NMR (400 MHz, $CDCl_3$) δ 7.45 – 7.57 (m, 2H), 7.74 – 7.80 (d, J = 13.8 Hz, 1H), 7.91 – 7.99 (m, 3H), 8.27 – 8.33 (d, J = 13.8, 1H).

(E)-3-(2-nitrovinyl)-1H-indole (3q)

Yellow solid. 40% yield. ^{1}H NMR (400 MHz, $CDCl_3$): δ 8.80 (s, 1H), 8.23 (d, J = 13.5 Hz, 1H), 7.77-7.71 (m, 2H), 7.61 (d, J = 2.9 Hz, 1H), 7.44-7.39 (m, 1H), 7.31-7.25 (m, 2H).

(E)-1,2-dichloro-4-((2-(2-nitrovinyl)phenoxy)methyl)benzene (4a)

Yellow solid. 85% yield. ^{1}H NMR (400 MHz, $CDCl_3$): δ 5.19 (s, 2H), 6.87 – 7.03 (m, 1H), 7.05 – 7.19 (m, 1H), 7.19 – 7.30 (m, 1H), 7.34 (d, J = 7.4 Hz, 1H), 7.40 – 7.53 (m, 2H), 7.61 (d, J = 7.4 Hz, 1H), 7.87 – 8.16 (m, 2H).

(E)-1-(benzyloxy)-2-(2-nitrovinyl)benzene (4b)

Yellow liquid. 81% yield. ^{1}H NMR (400 MHz, $CDCl_3$): δ 5.22 (s, 2 H), 7.0–7.05 (m, 2 H), 7.37–7.49 (m, 7 H), 7.85 (d, J = 13.6 Hz, 1 H), 8.2 (d, J = 13.6 Hz, 1 H).

(E)-1-nitro-2-((2-(2-nitrovinyl)phenoxy)methyl)benzene (4c)

Yellow liquid. 68% yield. ^{1}H NMR (400 MHz, $CDCl_3$): δ 5.24 (s, 2H), 6.85 – 7.02 (m, 1H), 7.11 – 7.17 (m, 1H), 7.20 – 7.32 (m, 1H), 7.36 – 7.52 (m, 1H), 7.61 (dq, J = 7.3, 2.4 Hz, 3H), 7.86 – 8.07 (m, 2H), 8.14 (dd, J = 6.7, 2.3 Hz, 1H).

(E)-1-((3-chlorobenzyl)oxy)-2-(2-nitrovinyl)benzene (4d)

Yellow liquid. 72% yield. ^{1}H NMR (400 MHz, $CDCl_3$): δ 5.19 (s, 2H), 6.87 – 7.10 (m, 2H), 7.17 – 7.28 (m, 1H), 7.33 (q, J = 5.5 Hz, 3H), 7.44 (s, 1H), 7.62 (d, J = 7.5 Hz, 1H), 8.02 (q, J = 15.1 Hz, 2H).

(E)-1,2-dichloro-4-((4-(2-nitrovinyl)phenoxy)methyl)benzene (4e)

Yellow liquid. 90% yield. ^{1}H NMR (400 MHz, $CDCl_3$): δ 5.22 (s, 2H), 6.83 (d, J = 7.3 Hz, 2H), 7.34 (d, J = 7.5 Hz, 1H), 7.38 – 7.52 (m, 2H), 7.58 (d, J = 7.3 Hz, 2H), 7.95 (d, J = 1.8 Hz, 2H).

General procedure for the synthesis of aldehyde 5a-e

To a stirred solution of saliciladheyde (for compound 5a-d) or p-hydroxybenzaldehyde (5e) in DMF, K2CO3 (2.5 equiv.) was added at room temperature. After 30 minutes, the appropriate benzyl chloride (0.9 equiv) was added and the mixture was reacted at 80 °C until desappearing of the starting materials as monitored by TLC (c.a. 2 h). After cooling at room temperature, the solvent was removed and the residues was resuspended in AcOEt. The organic phase was washed with an aqueous saturated solution of Na2CO3 and brine. The organic phase was dried over anh. Na2SO4 and concentrated to give the title product pure enough to be used in the next step without further purification.

2-((3,4-dichlorobenzyl)oxy)benzaldehyde (5a)

Coulorless liquid. ^{1}H NMR (400 MHz, DMSO-d6): δ 5.22 (s, 2H), 6.95 – 7.11 (m, 1H), 7.11 – 7.24 (m, 1H), 7.33 (d, J = 7.5 Hz, 1H), 7.39 – 7.60 (m, 3H), 7.81 (d, J = 7.7 Hz, 1H), 10.42 (s, 1H).

2-(benzyloxy)benzaldehyde (5b)

Coulorless liquid. ^{1}H NMR (400 MHz, $CDCl_3$): δ 10.56 (s, 1H), 7.85 (dd, J1 = 7.9 Hz, J2 = 1.8 Hz, 1H), 7.52 (ddd, J1 = 9.1 Hz, J2 = 7.5 Hz, J3 = 1.8 Hz, 1H), 7.46-7.31 (m, 5H), 7.06-7.00 (m, 2H), 5.18 (s, 2H).

2-((2-nitrobenzyl)oxy)benzaldehyde (5c)

White solid. ^{1}H NMR (400 MHz, $CDCl_3$): δ 10.59 (s, 1H), 8.21 (dd, 1H, J1=1.02 Hz, J2=1.05 Hz), 7.87-7.98 (m, 2H), 7.75 (t, 1H, J=15.5 Hz), 7.51-7.61 (m, 2H), 7.05 (m, 2H), 5.62 (s, 2H).

2-((3-chlorobenzyl)oxy)benzaldehyde (5d)

White solid. ^{1}H NMR (400 MHz, $CDCl_3$): δ 10.54 (s, 1H), 7.85 (dd, J1 = 7.7 Hz, J2 = 1.8 Hz, 1H), 7.52 (ddd, J1 = 9.2 Hz, J2 = 7.3 Hz, J3 = 1.8 Hz, 1H), 7.42 (s, 1H), 7.33-7.28 (m, 3H), 7.04 (t, J = 7.6 Hz, 1H), 6.99 (d, J = 8.4 Hz, 1H), 5.14 (s, 2H).

4-((3,4-dichlorobenzyl)oxy)benzaldehyde (5e)

Coulorless liquid. ^{1}H NMR (400 MHz, DMSO-d_6): δ 5.22 (s, 2H), 7.2 (d, 2H), 7.43 (m, 1H), 7.69 (d, 1H), 7.78 (s, 1H), 7.90 (d, 2H), 9.85 (s, 1H).

X-ray crystallography

*Tb*PTR1 was crystallized by the hanging-drop vapor diffusion technique at room temperature, as described elsewhere [35]. Briefly, well-ordered protein crystals grew within a few days (to final dimensions of ~ 600 µm x 200 µm x 50 µm) using a precipitant solution composed of 1.75-2.25 M sodium acetate and 0.1 M sodium citrate, pH 5. The complex *Tb*PTR1-cofactor-inhibitor was obtained by soaking crystals with the compound, to a final concentration of 4-5 mM (the compound was solubilized in DMSO and added without exceeding a DMSO:drop ratio of 1:9). After 30−60 min, crystals were transferred to the cryoprotectant solution (prepared by adding 30% v/v glycerol to the precipitant), and flash frozen in liquid nitrogen.

Diffraction images were collected using synchrotron radiation at the Diamond Light Source (DLS, Didcot, United Kingdom) beamline I03 equipped with a Eiger2 XE 16M detector. X-ray diffraction data were integrated using XDS [36] and scaled with SCALA [37] from the CCP4 software suite [38]. *Tb*PTR1 crystals belong to the monoclinic space group $P2_1$, with only slight variations in cell parameters among crystals. Data collection and processing statistics are reported in Table S1. The structure was solved by molecular replacement using the software Molrep [39] and a whole *Tb*PTR1 tetramer (PDB id 6TBX [40]) as search model, and it was subsequently refined with REFMAC5 [41]. The molecular graphic software Coot [42] was used for electron density inspection, model manipulation, and automatic placement of water molecules. The final model was inspected manually and checked with the programs Coot and Procheck [43]; refinement and validation statistics are summarized in Table S2. Coordinates and structure factors were validated and deposited in the PDB, under the accession code 8OF2. Figures were generated with CCP4 mg [44].

Molecular Modelling

Crystallographic structures of *Trypanosoma Brucei* PTR1 (*Tb*PTR1) available in Protein Data Bank (PDB) (https://www.rcsb.org/) were collected and ranked according to resolution (lower than 2 Å), structure integrity and the presence of a co-crystallized ligand in order to assess the mobility of the residues and determine relevant waters. The crystal complex of *Tb*PTR1-**Pyr** (PDB code: 7OPJ) was used for molecular docking analyses with Schrodinger LLC suite, version 2021-4 (Schrödinger LLC, NY, USA). Compounds (**1a**-**1q** and **2a**-**2e**) were built via builder panel in Maestro and subjected to ligand preparation using LigPrep module. The possible Lewis structures, tautomers and ionization states (pH 7.0 ± 2.0) for each of these compounds were generated and optimized with default settings. Stereoisomers computation was made by generating all combinations for the entire calculation (maximum 32 conformers/ligand). The protein was prepared using the Protein Preparation Workflow tool of GLIDE [28]: protein pre-process, optimization and minimization were performed to execute the correction of raw PDB structure. For docking simulations, the extra-precision (XP) protocol was adopted selecting co-crystallized **PYR** as centroid and setting a Van der Waals (vdW) radius scaling factor of 1.00, partial charge cutoff of 0.25, and OPLS4 force field. To verify the software capability of reproducing the co-crystallographic ligand binding poses, the cognate ligand PYR was extracted and self-docked to its corresponding binding site (Figure S1).

Biological Evaluation

Pteridine reductase inhibition assay

Recombinant *Tb*PTR1 and *Lm*PTR1 were produced in *E. coli* BL21(DE3) cells and purified by exploiting the N-terminal His^6-tag, according to established protocols [31]. The assay involves monitoring spectrophotometrically at 550 nm the reduction of cytochrome c Fe^{3+} to Fe^{2+} resulting from the oxidation of tetrahydrobiopterin H4B, a product of the enzymatic reaction catalyzed by PTR1, to quinoid dihydrobiopterin qH2B. In the presence of an inhibitor, the reduced catalytic activity of PTR1 leads to the formation of less H4B, which can become a substrate of the oxidation reaction catalyzed by cytochrome c Fe^{3+}. This results in the formation of a smaller amount of cytochrome c Fe^{2+} resulting in a reduced signal in the photometric reading. Inhibition of the PTR1 enzyme was evaluated in 20 mM citrate buffer at pH 6.0. The final reaction mixture contained the compound to be tested at the desired concentration, the *Tb*PTR1/*Lm*PTR1 enzyme (at 6.0 nM and 12 nM, respectively), H2B (0.3 µM/3 µM respectively), cytochrome c (100 µM in both cases), and NADPH (500 µM in both cases) in a total volume of 50 µL. The assay was conducted in 384 well plates; the test compounds (500 nL of 1 mM stock solutions in 100 % v/v DMSO for 10 µM final compound concentration and 1 % v/v DMSO) were added to each well followed by the addition of 45 µL of the reaction mixture (enzyme, H2B, cytochrome c in 20uM citrate buffer). A pre-reading of

the plate at 550 nm was performed using an EnVision® Multilabel Reader 2103 (PerkinElmer Inc, US) followed by incubation of the plate at 30 °C for 10 min. The enzymatic reaction was triggered by the addition of 5 µL of NADPH (from a 5 mM stock solution in ultrapure water) immediately beginning monitoring of the enzymatic reaction at 550 nm. Five readings are taken at 10, 20, 30, 40 and 50 min and the slope of the reaction curve is determined. The data are analyzed by Activity Base (IDBS, UK) and the 3-sigma method is applied to eliminate outliers in the control wells. Based on the slope, the data are normalized against the values obtained for methotrexate (positive control) and against a 1 % DMSO solution (negative control) allowing calculation of the percentage inhibition of each sample. The measurement at time zero was used to assess any optical interference in the sample [31,45].

In vitro evaluation of activity towards the *T. brucei* parasite

The efficacy of compounds against the *T. brucei* bloodstream forms was evaluated by modified resazurin assay [31]. *T. brucei* bloodstream forms were added to an equal volume of serial dilutions of the compound in HMI-9 medium until a cell density of 5 x10^3/mL was achieved. After incubation for 72 h at 37 °C and 5% CO_2, 20 µL of a 0.5 mM resazurin solution was added, and the plates were incubated for an additional 4 h under the same conditions. Fluorescence was measured at 540 nm and 620 nm (excitation and emission wavelengths, respectively) using a Synergy 2 Multi-Mode Reader (Biotek, USA). The anti-trypanosome effect was assessed by determining the IC_{50} value (concentration required to inhibit parasite growth by 50%) and calculated by nonlinear regression analysis using GraphPad Prism version 9 for Windows (GraphPad Software, USA). The reported IC_{50} values correspond to the average of the results obtained in at least three independent experiments.

In Vitro Evaluation of Activity against *L. infantum* Intramacrophage Amastigotes

The effect of the compounds on THP-1-derived macrophages was assessed by the MTT (3-(4,5-dimethylthiazol-2-yl)-2,5-diphenyl tetrazolium bromide) colorimetric assay. Briefly, 1x10^6 THP-1 cells were differentiated into macrophages with addition of 20 ng/mL phorbol-myristate 13-acetate (PMA) (Sigma-Aldrich, USA) for 18 h, followed by replacement with fresh medium for 24 h. Cells were incubated with the compound (concentration between 100 to 3 µM) after dilution in RPMI medium containing a maximum amount of 1 % v/v DMSO. After incubation for 72 h at 37 °C and 5 % CO_2, the medium was removed and 0.5 mg/mL MTT solution was added. The plates were incubated for an additional 4h to allow viable cells to transform MTT into purple formazan. Solubilization of formazan crystals was performed by adding 2-propanol upon supernatant removal, and absorbance was read at 570 nm using a Synergy 2 Multi-Mode reader (Biotek, USA).

Cytotoxicity was assessed by comparison with untreated cells and presented in the form of percentage of viability.

In vitro evaluation of activity towards the *T. cruzi* parasite

The assay is based on the determination of anti-parasitic activity on U2OS osteosarcoma cell lines infected with *T. cruzi*. U2OS cells were cultured in 6-well plates (3×10^6 HG39 cells/well) for 24 h and infected with tripomastigotes circulating in *T.cruzi* blood at a 1:1 ratio. After 4 h, cells were washed three times with PBS and fresh medium was added (RPMI supplemented with Glut/Pen/Strep and 20 % heat-inactivated FCS (Sigma-Aldrich, USA). Infected cells were incubated at 37 °C and 5 % CO_2. Twenty-four hours after infection, cells were treated with the compound and incubated for 72 h. Plates were analyzed by high content imaging and compound activity normalized relative to the control represented by infected and uninfected cells.

Evaluation of cytotoxicity toward THP-1 macrophages

The effect of the compounds on THP-1-derived macrophages was assessed by the MTT (3-(4,5-dimethylthiazol-2-yl)-2,5-diphenyl tetrazolium bromide) colorimetric assay. Briefly, 1×10^6 THP-1 cells were differentiated into macrophages with addition of 20 ng/mL phorbol-myristate 13-acetate (PMA) (Sigma-Aldrich, USA) for 18 h, followed by replacement with fresh medium for 24 h. Cells were incubated with the compound (concentration between 100 to 3 µM) after dilution in RPMI medium containing a maximum amount of 1 % v/v DMSO. After incubation for 72 h at 37 °C and 5 % CO_2, the medium was removed and 0.5 mg/mL MTT solution was added. The plates were incubated for an additional 4h to allow viable cells to transform MTT into purple formazan. Solubilization of formazan crystals was performed by adding 2-propanol upon supernatant removal, and absorbance was read at 570 nm using a Synergy 2 Multi-Mode reader (Biotek, USA). Cytotoxicity was assessed by comparison with untreated cells and presented in the form of percentage of viability.

Early ADME-Tox

Cardiotoxicity testing to *h*ERG

The Invitrogen Predictor™ *h*ERG Fluorescence Polarization assay was used in a 384-well plate format (#784076, Greiner Bio-One, AT) to test compounds. To each well of the plate, 100 nL of the compound (or control) was added followed by additions of 5 µl of a homogenized (undiluted) membrane solution followed by an additional 5 µl of tracer (1 nM: final concentration in the assay). Plates were incubated for 2 h at 25 °C in a humidity-controlled incubator and polarization

fluorescence was measured using an EnVision® Multilabel Reader 2103 (PerkinElmer Inc., USA). Data were analyzed using ActivityBase (IDBS, UK) and the 3-sigma method was applied for elimination of outliers from the control plate. Negative control (0 % inhibition) and positive control E-4031, an *h*ERG-type potassium channel blocker (100 % inhibition), were used to normalize the raw data. Each compound was tested in triplicate and IC_{50}, standard deviation, slope of the curve, minimum signal, and maximum signal for each dose-response curve were obtained using an XE module of ActivityBase (IDBS, UK).

Cytochrome P450 1A2, 2C9, 2C19, 2D6 and 3A4 inhibition assay

The P450-Glo™ luminescence-based assay (Promega, USA) was used in a 384-well format (#784076, Greiner Bio-One, AT) to test the compounds. The selected panel of cytochromes P450 includes microsomal preparation of cytochromes P450 1A2, 2C9, 2C19, 2D6, and 3A4 (Corning, USA) from baculovirus-infected insect cells (BTI-TN-5B1-4) expressing cytochrome P450 (CYP) and cytochrome c reductase (and cytochrome b5 for 3A4). Compounds (or controls) are added to an empty 384 well plate (100 nL with final concentration of 1 % v/v DMSO) using the Echo® Liquid Handler (Labcyte Inc., USA) then 5 µL/well of CYP/Luciferin-substrate is added and incubated for 30 min at 37 °C. The reaction is initiated by the addition of 5 µL/well of NADPH-containing mixture. After 30 min at 37°C the reaction with CYP is stopped and the luciferase reaction is started by the addition of 10 µL/well of Luciferin Detection Reagent. After 30 min at 37 °C the luminescence reading is taken using the Infinite® M1000 PRO plate reader (Tecan, CH). Outliers were removed using the 3-sigma method. Negative controls (0 % inhibition) include vehicle only (1 % v/v DMSO), standard specific CYP inhibitor: CYP1A2 inhibitor - α-naphtho-flavone (15 nM, Sigma-Aldrich, USA), CYP2C9 inhibitor - sulfaphenazole (67 nM, Sigma-Aldrich, USA), CYP2C19 inhibitor - troglitazone (3. 2 µM, Sigma-Aldrich, USA), CYP2D6 inhibitor - quinidine (2 nM, Sigma-Aldrich, USA) and CYP3A4 inhibitor - ketoconazole (54 nM, Sigma-Aldrich, USA) were used as positive controls (100 % inhibition). Each compound was tested in triplicate and IC_{50}, standard deviation, slope of the curve, minimum signal, and maximum signal for each dose-response curve were obtained using an XE module of ActivityBase (IDBS, UK).

A549 cell cytotoxicity assay

This assay was performed using the CellTiter-Glo assay from Promega Corp. A549 cells were obtained from DSMZ (German Collection of Microorganisms and Cell Cultures, Braunschweig, Germany). Cells were incubated at 37 °C in the presence of 5 % CO_2 and were harvested at 80-90 % confluence. Each compound tested (200 nl of 10 mM in 100 % v/v DMSO) was added to 384 well

cell culture plates (#781073, 384 CellStar, Greiner BioOne, AT) using the Echo 550® liquid handler (Labcyte Inc., USA). To collect cells, 1.5 mL of trypsin/EDTA (#L11-004, 0.5 mg/mL and 0.22 mg/mL respectively, PAA Laboratories GmbH, AT) per T175 vessel and incubated at 37 °C in the presence of 5 % CO_2 for 2 min. The isolated cells are then resuspended in pre-warmed medium to a density of 0.2 x 10^6 cells/mL. To this cell suspension, 20 µL per well is added to a 384 well plate until a final concentration of 100 µM and 0.1 % v/v DMSO is obtained. After 48 h incubation at 37 °C in the presence of 5 % CO_2, 20 µL CellTiter-Glo® reagent (#G7571, Promega Inc., USA) was added per well and the plate was placed on a linear shaker for one min at room temperature and further incubated at room temperature without mechanical agitation for 10 min. Luminescence reading was performed using the EnVision® Multilabel Reader 2103 (PerkinElmer Inc., USA) with 0.5 second reading time per well. Each plate also contained 16 wells for the positive control (cells prepared by treating with cisplatin: 200 nL of a 300 mM stock solution in 100% v/v DMSO to achieve a final concentration of 3 mM cisplatin). The 16 wells for each plate with the negative control were prepared by treating the cells with DMSO alone (200 nL). Each compound was tested in triplicate and IC_{50}, standard deviation, slope of the curve, minimum signal, and maximum signal for each dose-response curve were obtained using an XE module of ActivityBase (IDBS, UK).

Evaluation of pharmacokinetics by SNAP-PK

Compounds **1m**, **1o**, **1p**, **2a**, **2d**, and **2e** were mixed with hydroxypropyl-β-cyclodextrins (50 % w/v) (Cavasol® W7 HP Pharma, Ashland, USA) to increase their solubility by and bioavailability for subsequent pharmacokinetic studies through the formation of water -soluble inclusion complexes. The pharmacokinetics of compounds **1m**, **1o**, **1p**, **2a**, **2d**, and **2e** in plasma were determined by the SNAP-PK technique. The compounds were administered at 20 mg/kg complexed with cyclodextrins to 6 BALB/c mice/compound. At 30, and 45 min and 1, 2, 3, 5 and 24 hours after administration blood was collected by tail vein puncture. Plasma was separated from blood and stored at -80ºC until analysis. LC-MS/MS was used for quantification of the compound in plasma.

Data analysis and Software's

Each docking experiment was repeated twice to guarantee the reproducibility of the pose. Van der Waals (vdW) radius scaling factor of 1.00, partial charge cutoff of 0.25, and OPLS4 force field were employed for XP protocol.

For the IC_{50} calculation, each sample is tested in triplicate and the values of IC_{50}, standard deviation, slope, minimum signal, and maximum signal for each dose-response curve were obtained by employing a 4-parameter logistic (4-PL) calculation in the XE module of ActivityBase (IDBS, UK).

EC and CC_{50} were calculated by nonlinear regression analysis using GraphPad Prism version 5.00 for Windows (GraphPad Software, USA). Each compound was tested in triplicate against hERG, cytochromes and A549 cell**,** and IC_{50}, standard deviation, slope of the curve, minimum signal, and maximum signal for each dose-response curve were obtained using an XE module of ActivityBase (IDBS, UK). All IC_{50} values for these enzymes are associated with a standard deviation <10 %.

LC-MS/MS analysis method was validated after building a regression curve in duplicate, with the calculation of LOD, LOQ, accuracy and precision.

The Heatmaps in Figure 10 are obtained with Excel 2022 with the option 'conditional formatting' > 'three-color scale'. Lower values were represented with #F8696B (RBD) colour (red), higher values with #63BE7B (RGB) colour (green), while opaque white #FFFBE7 (RBD) was employed to represent the 50% of the colour interval for map **a**, and at 10% of the colour interval for map **b**.

Acknowledgments

The Authors would like to acknowledge Diamond Light Source (DLS) for beamtime (proposal MX21741) and the staff of beamline I03. The Authors would also like to thank all staff members of the synchrotron facilities for their assistance in using the beamlines and Centro Interdipartimentale Grandi Strumenti (CIGS) of the University of Modena and Reggio Emilia.

Funding

The present work was funded by the This project has received funding from the European Union's Seventh Framework Programme for research, technological development, and demonstration under the grant agreement n◦603240 (NMTrypI, New Medicine for Trypanosomatidic Infections). This research was realized within the European COST Action 21111 "One Health drugs against parasitic vector borne diseases in Europe and beyond" (OneHealth*drugs*); www.onehealthdrugs.com.

Declaration of competing interest

The authors declare that they have no known competing financial interests or personal relationships that could have appeared to influence the work reported in this paper.

Data availability

The raw data employed in this paper are reported in the Supplementary Information when not stated in the Main Text.

References

[1] M.A. Pereira, G. Santos-Gomes, Parasitic Infection and Immunity—A Special Biomedicines Issue, Biomedicines. 10 (2022) 2547. https://doi.org/10.3390/biomedicines10102547.

[2] A.P. Maurice, A. Jenkin, R.E. Norton, A. Hamilton, Y.-H. Ho, Epidemiology of Parasitic Diseases, in: Surg. Manag. Parasit. Dis., Springer International Publishing, Cham, 2020: pp. 3–21. https://doi.org/10.1007/978-3-030-47948-0_1.

[3] M.P. Barrett, S.L. Croft, Management of trypanosomiasis and leishmaniasis, Br. Med. Bull. 104 (2012) 175–196. https://doi.org/10.1093/bmb/lds031.

[4] D. Horn, A profile of research on the parasitic trypanosomatids and the diseases they cause, PLoS Negl. Trop. Dis. 16 (2022) e0010040. https://doi.org/10.1371/journal.pntd.0010040.

[5] WHO - Human African trypanosomiasis (sleeping sickness). https://www.who.int/data/gho/data/themes/topics/human-african-trypanosomiasis (accessed Mar 08, 2022)., (n.d.).

[6] B. Zulfiqar, T.B. Shelper, V.M. Avery, Leishmaniasis drug discovery: recent progress and challenges in assay development, Drug Discov. Today. 22 (2017) 1516–1531. https://doi.org/10.1016/j.drudis.2017.06.004.

[7] P. Kaye, P. Scott, Leishmaniasis: complexity at the host–pathogen interface, Nat. Rev. Microbiol. 9 (2011) 604–615. https://doi.org/10.1038/nrmicro2608.

[8] WHO. Elimination of Human African Trypanosomiasis as public health problem. Weekly epidemiological record. No.21, 28 May 2021., (n.d.).

[9] A.K. Lindner, V. Lejon, F. Chappuis, J. Seixas, L. Kazumba, M.P. Barrett, E. Mwamba, O. Erphas, E.A. Akl, G. Villanueva, H. Bergman, P. Simarro, A. Kadima Ebeja, G. Priotto, J.R. Franco, New WHO guidelines for treatment of gambiense human African trypanosomiasis including fexinidazole: substantial changes for clinical practice, Lancet Infect. Dis. 20 (2020) e38–e46. https://doi.org/10.1016/S1473-3099(19)30612-7.

[10] I. Kuepfer, E.P. Hhary, M. Allan, A. Edielu, C. Burri, J.A. Blum, Clinical Presentation of T.b. rhodesiense Sleeping Sickness in Second Stage Patients from Tanzania and Uganda, PLoS Negl. Trop. Dis. 5 (2011) e968. https://doi.org/10.1371/journal.pntd.0000968.

[11] K. Ndung'u, G.A. Murilla, J.K. Thuita, G.N. Ngae, J.E. Auma, P.K. Gitonga, D.K. Thungu,

R.K. Kurgat, J.K. Chemuliti, R.E. Mdachi, Differential virulence of Trypanosoma brucei rhodesiense isolates does not influence the outcome of treatment with anti-trypanosomal drugs in the mouse model, PLoS One. 15 (2020) e0229060. https://doi.org/10.1371/journal.pone.0229060.

[12] P.G. Kennedy, Clinical features, diagnosis, and treatment of human African trypanosomiasis (sleeping sickness), Lancet Neurol. 12 (2013) 186–194. https://doi.org/10.1016/S1474-4422(12)70296-X.

[13] D. Kaba, M. Koffi, L. Kouakou, E.K. N'Gouan, V. Djohan, F. Courtin, M.K. N'Djetchi, B. Coulibaly, G.P. Adingra, D. Berté, B.T.D. Ta, M. Koné, B.M. Traoré, S.A. Sutherland, R.E. Crump, C.-I. Huang, J. Madan, P.R. Bessell, A. Barreaux, P. Solano, E.H. Crowley, K.S. Rock, V. Jamonneau, Towards the sustainable elimination of gambiense human African trypanosomiasis in Côte d'Ivoire using an integrated approach, PLoS Negl. Trop. Dis. 17 (2023) e0011514. https://doi.org/10.1371/journal.pntd.0011514.

[14] E. Pays, M. Radwanska, S. Magez, The Pathogenesis of African Trypanosomiasis, Annu. Rev. Pathol. Mech. Dis. 18 (2023) 19–45. https://doi.org/10.1146/annurev-pathmechdis-031621-025153.

[15] P. Vincendeau, B. Bouteille, Immunology and immunopathology of African trypanosomiasis, An. Acad. Bras. Cienc. 78 (2006) 645–665. https://doi.org/10.1590/S0001-37652006000400004.

[16] A. Venturelli, L. Tagliazucchi, C. Lima, F. Venuti, G. Malpezzi, G.E. Magoulas, N. Santarem, T. Calogeropoulou, A. Cordeiro-da-Silva, M.P. Costi, Current Treatments to Control African Trypanosomiasis and One Health Perspective, Microorganisms. 10 (2022) 1298. https://doi.org/10.3390/microorganisms10071298.

[17] A. Ponte-Sucre, F. Gamarro, J.-C. Dujardin, M.P. Barrett, R. López-Vélez, R. García-Hernández, A.W. Pountain, R. Mwenechanya, B. Papadopoulou, Drug resistance and treatment failure in leishmaniasis: A 21st century challenge., PLoS Negl. Trop. Dis. 11 (2017) e0006052. https://doi.org/10.1371/journal.pntd.0006052.

[18] G. Cullia, L. Tamborini, P. Conti, C. De Micheli, A. Pinto, Folates in *Trypanosoma brucei* : Achievements and Opportunities, ChemMedChem. 13 (2018) 2150–2158. https://doi.org/10.1002/cmdc.201800500.

[19] G. Tassone, G. Landi, P. Linciano, V. Francesconi, M. Tonelli, L. Tagliazucchi, M.P. Costi, S. Mangani, C. Pozzi, Evidence of Pyrimethamine and Cycloguanil Analogues as Dual Inhibitors of Trypanosoma brucei Pteridine Reductase and Dihydrofolate Reductase, Pharmaceuticals. 14 (2021) 636. https://doi.org/10.3390/ph14070636.

[20] S. Dean, Basic Biology of Trypanosoma brucei with Reference to the Development of Chemotherapies, Curr. Pharm. Des. 27 (2021) 1650–1670. https://doi.org/10.2174/1381612827666210119105008.

[21] M.P. Kimuda, D. Laming, H.C. Hoppe, Ö. Tastan Bishop, Identification of Novel Potential Inhibitors of Pteridine Reductase 1 in Trypanosoma brucei via Computational Structure-Based Approaches and in Vitro Inhibition Assays, Molecules. 24 (2019) 142. https://doi.org/10.3390/molecules24010142.

[22] G.M. das Neves, L.P. Kagami, I.L. Gonçalves, V.L. Eifler-Lima, Targeting pteridine reductase 1 and dihydrofolate reductase: the old is a new trend for leishmaniasis drug discovery, Future Med. Chem. 11 (2019) 2107–2130. https://doi.org/10.4155/fmc-2018-0512.

[23] A. Dawson, F. Gibellini, N. Sienkiewicz, L.B. Tulloch, P.K. Fyfe, K. McLuskey, A.H. Fairlamb, W.N. Hunter, Structure and reactivity of Trypanosoma brucei pteridine reductase: inhibition by the archetypal antifolate methotrexate, Mol. Microbiol. 61 (2006) 1457–1468. https://doi.org/10.1111/j.1365-2958.2006.05332.x.

[24] A.I. Khalaf, J.K. Huggan, C.J. Suckling, C.L. Gibson, K. Stewart, F. Giordani, M.P. Barrett, P.E. Wong, K.L. Barrack, W.N. Hunter, Structure-Based Design and Synthesis of Antiparasitic Pyrrolopyrimidines Targeting Pteridine Reductase 1, J. Med. Chem. 57 (2014) 6479–6494. https://doi.org/10.1021/jm500483b.

[25] C. Pozzi, G. Tassone, S. Mangani, X-ray Crystallography Contributions to Drug Discovery Against Parasite, in: 2018: pp. 175–230. https://doi.org/10.1016/bs.armc.2018.08.005.

[26] A.W. Schüttelkopf, L.W. Hardy, S.M. Beverley, W.N. Hunter, Structures of Leishmania major Pteridine Reductase Complexes Reveal the Active Site Features Important for Ligand Binding and to Guide Inhibitor Design, J. Mol. Biol. 352 (2005) 105–116. https://doi.org/10.1016/j.jmb.2005.06.076.

[27] G. Landi, P. Linciano, C. Borsari, C.P. Bertolacini, C.B. Moraes, A. Cordeiro-da-Silva, S.

Gul, G. Witt, M. Kuzikov, M.P. Costi, C. Pozzi, S. Mangani, Structural Insights into the Development of Cycloguanil Derivatives as *Trypanosoma brucei* Pteridine-Reductase-1 Inhibitors, ACS Infect. Dis. 5 (2019) 1105–1114. https://doi.org/10.1021/acsinfecdis.8b00358.

[28] T.A. Halgren, R.B. Murphy, R.A. Friesner, H.S. Beard, L.L. Frye, W.T. Pollard, J.L. Banks, Glide: A New Approach for Rapid, Accurate Docking and Scoring. 2. Enrichment Factors in Database Screening, J. Med. Chem. 47 (2004) 1750–1759. https://doi.org/10.1021/jm030644s.

[29] A.C. Wallace, R.A. Laskowski, J.M. Thornton, LIGPLOT: a program to generate schematic diagrams of protein-ligand interactions, "Protein Eng. Des. Sel. 8 (1995) 127–134. https://doi.org/10.1093/protein/8.2.127.

[30] S. Yuan, H.C.S. Chan, Z. Hu, Using <scp>PyMOL</scp> as a platform for computational drug design, WIREs Comput. Mol. Sci. 7 (2017). https://doi.org/10.1002/wcms.1298.

[31] C. Borsari, R. Luciani, C. Pozzi, I. Poehner, S. Henrich, M. Trande, A. Cordeiro-da-Silva, N. Santarem, C. Baptista, A. Tait, F. Di Pisa, L. Dello Iacono, G. Landi, S. Gul, M. Wolf, M. Kuzikov, B. Ellinger, J. Reinshagen, G. Witt, P. Gribbon, M. Kohler, O. Keminer, B. Behrens, L. Costantino, P. Tejera Nevado, E. Bifeld, J. Eick, J. Clos, J. Torrado, M.D. Jiménez-Antón, M.J. Corral, J.M. Alunda, F. Pellati, R.C. Wade, S. Ferrari, S. Mangani, M.P. Costi, Profiling of Flavonol Derivatives for the Development of Antitrypanosomatidic Drugs, J. Med. Chem. 59 (2016) 7598–7616. https://doi.org/10.1021/acs.jmedchem.6b00698.

[32] S. André, V. Rodrigues, S. Pemberton, M. Laforge, Y. Fortier, A. Cordeiro-da-Silva, J. MacDougall, J. Estaquier, Antileishmanial Drugs Modulate IL-12 Expression and Inflammasome Activation in Primary Human Cells, J. Immunol. 204 (2020) 1869–1880. https://doi.org/10.4049/jimmunol.1900590.

[33] A. Buschini, L. Ferrarini, S. Franzoni, S. Galati, M. Lazzaretti, F. Mussi, C. Northfleet de Albuquerque, T. Maria Araújo Domingues Zucchi, P. Poli, Genotoxicity Revaluation of Three Commercial Nitroheterocyclic Drugs: Nifurtimox, Benznidazole, and Metronidazole, J. Parasitol. Res. 2009 (2009) 1–11. https://doi.org/10.1155/2009/463575.

[34] M. Montenegro, C. Cuervo, C. Cardenas, S. Duarte, J.R. Díaz, M.C. Thomas, M.C. Lopez, C.J. Puerta, Identification of a type I nitroreductase gene in non-virulent Trypanosoma rangeli, Mem. Inst. Oswaldo Cruz. 112 (2017) 504–509. https://doi.org/10.1590/0074-

02760160532.

[35] F. Di Pisa, G. Landi, L. Dello Iacono, C. Pozzi, C. Borsari, S. Ferrari, M. Santucci, N. Santarem, A. Cordeiro-da-Silva, C. Moraes, L. Alcantara, V. Fontana, L. Freitas-Junior, S. Gul, M. Kuzikov, B. Behrens, I. Pöhner, R. Wade, M. Costi, S. Mangani, Chroman-4-One Derivatives Targeting Pteridine Reductase 1 and Showing Anti-Parasitic Activity, Molecules. 22 (2017) 426. https://doi.org/10.3390/molecules22030426.

[36] W. Kabsch, *XDS*, Acta Crystallogr. Sect. D Biol. Crystallogr. 66 (2010) 125–132. https://doi.org/10.1107/S0907444909047337.

[37] P.R. Evans, An introduction to data reduction: space-group determination, scaling and intensity statistics., Acta Crystallogr. D. Biol. Crystallogr. 67 (2011) 282–92. https://doi.org/10.1107/S090744491003982X.

[38] M.D. Winn, C.C. Ballard, K.D. Cowtan, E.J. Dodson, P. Emsley, P.R. Evans, R.M. Keegan, E.B. Krissinel, A.G.W. Leslie, A. McCoy, S.J. McNicholas, G.N. Murshudov, N.S. Pannu, E.A. Potterton, H.R. Powell, R.J. Read, A. Vagin, K.S. Wilson, Overview of the *CCP* 4 suite and current developments, Acta Crystallogr. Sect. D Biol. Crystallogr. 67 (2011) 235–242. https://doi.org/10.1107/S0907444910045749.

[39] A. Vagin, A. Teplyakov, Molecular replacement with *MOLREP*, Acta Crystallogr. Sect. D Biol. Crystallogr. 66 (2010) 22–25. https://doi.org/10.1107/S0907444909042589.

[40] G. Landi, P. Linciano, G. Tassone, M.P. Costi, S. Mangani, C. Pozzi, High-resolution crystal structure of *Trypanosoma brucei* pteridine reductase 1 in complex with an innovative tricyclic-based inhibitor, Acta Crystallogr. Sect. D Struct. Biol. 76 (2020) 558–564. https://doi.org/10.1107/S2059798320004891.

[41] G.N. Murshudov, P. Skubák, A.A. Lebedev, N.S. Pannu, R.A. Steiner, R.A. Nicholls, M.D. Winn, F. Long, A.A. Vagin, *REFMAC* 5 for the refinement of macromolecular crystal structures, Acta Crystallogr. Sect. D Biol. Crystallogr. 67 (2011) 355–367. https://doi.org/10.1107/S0907444911001314.

[42] P. Emsley, B. Lohkamp, W.G. Scott, K. Cowtan, Features and development of *Coot*, Acta Crystallogr. Sect. D Biol. Crystallogr. 66 (2010) 486–501. https://doi.org/10.1107/S0907444910007493.

[43] R.A. Laskowski, M.W. MacArthur, D.S. Moss, J.M. Thornton, PROCHECK: a program to

check the stereochemical quality of protein structures, J. Appl. Crystallogr. 26 (1993) 283–291. https://doi.org/10.1107/S0021889892009944.

[44] S. McNicholas, E. Potterton, K.S. Wilson, M.E.M. Noble, Presenting your structures: the *CCP* 4 *mg* molecular-graphics software, Acta Crystallogr. Sect. D Biol. Crystallogr. 67 (2011) 386–394. https://doi.org/10.1107/S0907444911007281.

[45] M. Santucci, R. Luciani, E. Gianquinto, C. Pozzi, F. di Pisa, L. Dello Iacono, G. Landi, L. Tagliazucchi, S. Mangani, F. Spyrakis, M.P. Costi, Repurposing the Trypanosomatidic GSK Kinetobox for the Inhibition of Parasitic Pteridine and Dihydrofolate Reductases., Pharmaceuticals (Basel). 14 (2021). https://doi.org/10.3390/ph14121246.